

Problems

- Problem 12.1** What is the meaning of the reconnection velocity V_{rec} in Eq. (12.2)?
- Problem 12.2** Give an explanation for the Lundqvist number S .
- Problem 12.3** Why can the reconnection efficiency be expressed through the parallel electric field like done in Eq. (12.5)?
- Problem 12.4** Reconnection makes sense for Mach numbers $M_A < 1$ only. Why?
- Problem 12.5** Why does Petschek reconnection with its localised diffusivity need discontinuities outside the X point, while Parker reconnection does not?
- Problem 12.6** Discuss the different terms in Ohm's law Eq. (12.7) in full depth. Explain the drawing in Fig. 12.2.
- Problem 12.7** What does it mean that only the electrons are frozen while the ions are not?
- Problem 12.8** Derive Eqs. (12.9–10) and (12.13). Explain which terms survive for discussion of reconnection.
- Problem 12.9** Explain the drawing in Fig. 12.3.
- Problem 12.10** Electron inertia has been claimed to contribute substantially to reconnection. Why is it nevertheless of little importance, even though Eq. (12.17) is correct? Or, if important, than where and for what reason?
- Problem 12.11** Explain the different terms in Eq. (12.2). What do you believe contributes to the ponderomotive force? Why does fluid turbulence not contribute or when, and in what sense?
- Problem 12.12** Guess the role of guide fields in reconnection. Why is a guide field parallel to the neutral sheet current more important in driving reconnection than a transverse guide field? What do you believe is the latter doing?
- Problem 12.13** Explain the absence of Hall currents in a pair plasma. Why does one need to include relativity when dealing with electron positron pairs? Can pair plasmas of this kind be considered to be cold?
- Problem 12.14** Derive Eq. (12.26) and explain its content.
- Problem 12.15** Use the numbers given in the description of Fig. 12.9 and estimate the anomalous resistivity by using the wave power of lower hybrid waves given in Chapters 10 and 11. Assume that the anomalous collision frequency is given by $\nu_e = \omega_{pe} W_w / nk_B T$. Is this sufficient for initiating reconnection, and when, then under which condition?
- Problem 12.16** Explain the content of Fig. 12.16 in detail. Why is it relevant for tail reconnection? Why is it not relevant for magnetopause reconnection?

— 13 —

Collisionless Shocks

This last chapter of the present volume is devoted to one of the most important applications of kinetic wave theory in space plasma physics: the physics of collisionless shocks. In previous chapters we have already talked several times about shocks in plasmas, there however only from the viewpoint of fluid theory, which cannot give any clue to the interior, generation, or general behaviour of shocks and all the processes it may trigger in the environmental plasmas. We will resolve this deficiency – at least in part – in this chapter, where we are going to apply some of the knowledge we have accumulated in the three last chapters on the complicated physics of waves in a collisionless plasma.

One may, in this context, at the beginning stumble across the term *collisionless* shock which seems to be a contradiction in itself. If something is shocked then it is probably by collisions, isn't it? True, this may hold in real life. But plasmas exhibit a strange behaviour, as we have shown in many cases, in as far as even in the complete absence of collisions they behave as if collisions would act in the plasma. The reason, we have elucidated, is that plasmas contain long-range interactions which are provided by the electromagnetic field acting on the charged particle component. These long-range actions provide correlations and force the particles into enslavement. Particles are not really free in plasmas; they have to follow the dictatorship of the fields, even when these fields have been generated by the particles themselves as a consequence of their own dynamics under the action of the Lorentz force.

Shocks in a collisionless plasma can evolve in two ways. One is the case we are already familiar with: when a large obstacle stands in the flow, which the flow is unable to push away. If the Mach number of the flow as seen in the frame of the obstacle is $M_{ns} > 1$, then the flow will evolve a shock wave in front of the obstacle. In principle this is also the case when a blast wave expands into the flow from an explosion like a solar flare or solar mass ejection, the impact of a large asteroid or comet on one of the planets, or an atomic explosion. One then only has to change the frame in order to see the similarity. The driver of the blast is the extended obstacle, whose speed relative to the flow is super-magnetosonic and the flow heads against the driver, creating the blast shock in front of the driver.

We have also become familiar with the other possibility when speaking of instability and wave growth. This growth of the wave may only be local, and then the wave itself evolves into a large-amplitude localised entity, with steep flanks which may exhibit shock behaviour. In the other case, when the wave is substantially faster or slower than the flow, it presents an obstacle to the flow. The last case happens, for instance, when a wave flows against a fast flow with speed large enough to exceed the

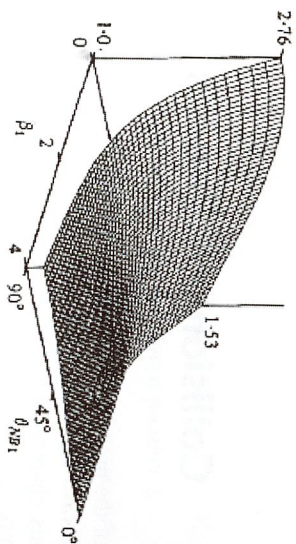


Figure 13.1: The dependence of the critical magnetohydrodynamic Mach number for dissipative shocks on the upstream shock-normal angle, Θ_{Bn} , and on the upstream plasma, β_1 . The critical Mach number is a strong function of the latter and Θ_{Bn} maximising for perpendicular shocks, $\Theta_{Bn} = 90^\circ$, and cold upstream flow and can become quite small otherwise (courtesy of the American Geophysical Society).

flow speed even slightly and thus has large Mach number in the flow frame. In both cases shocks evolve as well. In the latter case, however, those shocks will be relatively slow, just exceeding the Mach number bound above which shocks evolve. Such shocks are *subcritical* in contrast to blast wave shocks which are mostly *super-critical*. We may thus distinguish between these two classes. In the following, we briefly discuss subcritical shocks before switching to the more interesting super-critical shocks, the discussion of which will occupy most of this chapter and of which the Earth's bow shock is the most distinguished and best investigated example in the entire Universe.

13.1 Subcritical Shocks

An important property of collisionless shocks is their criticality. Subcritical shocks have Mach numbers, $M < M_c$, less than critical. Criticality refers to the capability of a shock wave to maintain its shock character solely by resistive (Joule) dissipation. Since collisionless shocks are free of binary interaction between the particles, criticality is defined with respect to some Joule dissipation. In this sense, criticality is defined implicitly: a collisionless shock that does not generate any Joule dissipation is super-critical for all Mach numbers $M > 1$. Usually, a collisionless shock generates some weak dissipation, however. Therefore, it makes sense to define a largest critical Mach number, M_c , by assuming that the Mach number downstream of the shock should not be larger than unity, implying that the downstream plasma cannot be further heated by any dissipation. Hence, from the magnetohydrodynamic Rankine–Hugoniot jump relations putting the downstream Mach number $M = 1$ defines the critical upstream Mach number. The numerically determined *largest* critical Mach number is

$$M_c \approx 2.76. \quad (13.1)$$

The dependence of the critical Mach number on plasma, β and Θ_{Bn} , is shown in Fig. 13.1. Critical Mach numbers are small and decrease with increasing shock normal

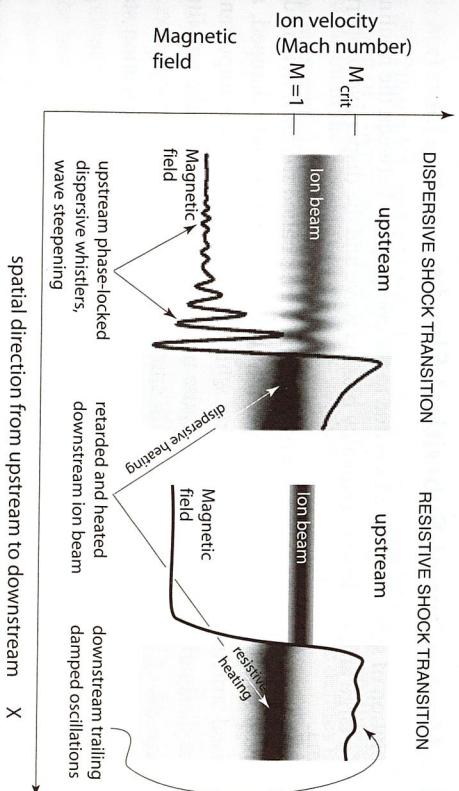


Figure 13.2: Two types of subcritical shocks in ion phase space and magnetic field profile. dispersively dominated (left) and dissipatively dominated (right). The dispersive shock has upstream whistlers attached, being a nonlinear whistler itself. The upstream ion flow is subcritical. Retarding the flow in the shock is dominated by dispersive effects. In resistive shock transition, the shock forms a steep ramp lacking upstream oscillations. Heating and retarding is due to Joule heating. Downstream the magnetic field may evolve trailing oscillations.

angle, Θ_{Bn} . Some of the shocks of very low Mach number in the solar wind are subcritical, but in general the shocks in the heliosphere, and in particular Earth's bow shock, are super-critical, with their Mach numbers exceeding the critical Mach number. For instance, the bow shock has canonical Mach number of $5 < M < 12$, with the most probable value around $M = 8$.

In subcritical shocks the co-operation of dissipation inside the shock front and dispersion of waves is sufficient for providing the necessary dissipation/dispersion of sustaining the shock transition from upstream to the downstream flow. For illustration, Fig. 13.2 shows two schematic subcritical shock profiles, one of them a dispersion dominated shock transition resulting from nonlinear steepening of waves (in this case whistlers), the other the extreme case of a purely resistive shock transition.

Dispersion alone cannot create a shock transition. It produces some kind of localised wave, like the various kinds of solitary waves and BGK modes we will briefly note below. These are all structures that are connected with local electric potential wells. Depending on the polarity of these potentials they reflect one sort of particle out of the upstream low energy component while they trap and accelerate particles from the other component. Hence, in the complete absence of any kind of dissipation, a subcritical 'shock' can exist only when it reflects and traps some particles. Then, however, it is a marginal case of shock, a non-dissipative structure which by definition is reversible. Such structures belong to the family of solitary waves. If this is not the case, the subcritical shock must be capable of generating some collisionless dissipation even when it is dominated by dispersion like in the first case shown.

13.1.1 Mechanism of Subcritical Shocks

The evolution of subcritical shocks is due to the competition between the nonlinear steepening of a large amplitude low frequency plasma wave and the dispersive properties of the plasma.

Dispersion can lead to the formation of localised waves called *solitons*. In a medium that contains a small amount of dissipation the waves become weakly damped, and these localised structures evolve into a ramp which mimics a shock. It is important to note that the dissipation is in many cases quite unimportant, as long as the amplitude and the steepness of the wave packet remain small. However, when both increase, the gradient scale enters the scale of local dissipative interactions, and dissipation starts becoming important.

Wave Steeping in Dispersion Dominated Shocks

There is no problem with the understanding of dispersion in plasma. Shock waves grow out of waves that are generated in the impact of the super-magnetosonic flow onto the obstacle. The obstacle reflects ions back upstream, thus creating an ion-ion beam situation which is unstable with respect to low-frequency magnetosonic waves propagating upstream with velocity V away from the obstacle. Under collisionless conditions their velocity evolves with time according to

$$dV/dt = (\partial V/\partial t) + V\partial V/\partial x = 0. \quad (13.2)$$

During propagation, the main effect on the shape of a sinusoidal disturbance, $V \sim \sin k(x - c_{ms}t)$, comes from the action of the nonlinear term. This term can be written as $Vk \cos k(x - c_{ms}t)$. Inserting for V this becomes $\sim \frac{1}{2} \sin 2k(x - c_{ms}t)$.

Harmonic sidebands of half wavelength and half the amplitude are generated, which, by the same mechanism, also generate sidebands on their own, now at quarter original wavelength and amplitude, and so on, with increasingly shorter wavelengths. The total amplitude is the superposition of all these sideband harmonics which propagate at the same magnetosonic velocity, c_{ms} . They superimpose locally and add to the wave amplitude, causing the wave to steepen until the gradient lengths become so short that dissipation takes over. If this does not happen, the wave will turn over and break like water waves do when running against the beach. In the other case, when dispersion lets the shorter wavelength waves escape from the transition, wave steepening is arrested at a maximum wave amplitude and minimum wavelength.

We refer to a one-dimensional cold ($\beta_1 \ll 1$) two fluid damped model of a stationary magnetosonic wave in pressure balance,

$$\nabla_x B_z = \mu_0 e n v_y, \quad \nabla_x E_y = 0, \quad \nabla_x n v_x = 0, \quad (13.3)$$

$$\nabla_x \left(\frac{1}{2} m_i n v_x^2 + \frac{B_z^2}{2\mu_0} \right) = 0, \quad m_e n v_x \nabla_x v_y = -e n E_y + e n v_x B_z - V_{am} m_e n v_y.$$

We now define $\xi = x/\lambda_e$. Transforming to the shock velocity frame V_{sh} , one obtains

$$\frac{d^2 b}{d\xi^2} = b - 1 + Ab(1 - b^2) - a \frac{db}{d\xi}, \quad (13.4)$$

13.1. Subcritical Shocks

with $b(x) \equiv B_z(x)/B_1$, the ratio of the magnetic field to the upstream magnetic field, $A \equiv B_1^2/(2\mu_0 m_i V_{sh}^2)$, and $a \equiv v\lambda_e/V_{sh}$. This equation can be identified as the equation of motion of a hypothetical particle with coordinate b and time ξ , including frictional dissipation in the first derivative. In the absence of dissipation, one defines the Sagdeev pseudo-potential $S(b)$:

$$2S(b) = (b-1)^2 [A(b+1)^2 - 2], \quad b < b_{max} = (2V_{sh}/V_{A1}) - 1. \quad (13.5)$$

Negative values of $S(b)$ constitute a potential trough for the hypothetical particle if the field amplitudes, $b < b_{max}$, are smaller than a maximum value, b_{max} . For a given $S(b)$, the hypothetical particle performs a stationary oscillation in this potential trough, with amplitude equal to the distance between the walls. The shape of the trough is shown as the heavy line marked $s = 0$ on the right in Fig. 13.3 for the special case $M_A = 1.6$. The maximum possible amplitude is reached for $S(b) = 0$. The ratio $V_{sh}/V_{A1} = \mathcal{M}_{sh}$ is the shock-Mach number, i.e., the Mach number of the possible stationary solutions in this dissipationless case. Including the resistive damping, this amplitude decreases during the oscillation and the pseudo-particle will ultimately settle in the final state at the minimum of the pseudo-potential, $S(b)$. The Sagdeev potential minimum is at the stationary downstream value of the normalised magnetic field,

$$2b(S_{min}) \equiv 2b_2 = (1 + 8\mathcal{M}_{sh}^2)^{\frac{1}{2}} - 1. \quad (13.6)$$

It corresponds to the final stationary shock state of a subcritical fast magnetosonic shock. It is independent of the dissipation even though it has been reached only due to the action of the anomalous dissipation, a .

A shock of this kind is a weak shock since the plasma pressure contribution has been neglected and the plasma has been assumed to be cold, such that the heating of the plasma by the shock itself is also small and does not appear anywhere. The shock profile can be determined from the solution of the equation for b . It is found to be a spatial oscillation, reaching maximum at the shock ramp and decreasing exponentially behind the shock with spatially damped amplitude, $b(\xi) \sim \exp(-a\xi) \sin(\xi \sqrt{M_{sh} - 1})$. Because of the simplifying assumptions this solution holds only for small shock amplitudes. At large dissipation one obtains instead a non-oscillating shock ramp, the cases shown in Fig. 13.2.

13.1.2 Causes of Anomalous Dissipation

Dissipation sets on when the scale of steepness of the wave compares to the dissipation scale, L_d . Then, in the evolution equation of the velocity, the next higher order derivatives with respect to x cannot be neglected anymore, yielding

$$dV/dt = (\partial V/\partial t) + V\nabla_x V = \nabla_x D\nabla_x V - \beta \nabla_x^3 V + \dots, \quad (13.7)$$

now with non-vanishing right-hand side. The first of the new terms is second-order in the gradient, ∇_x , and corresponds to the anomalous diffusion. The second (third-order

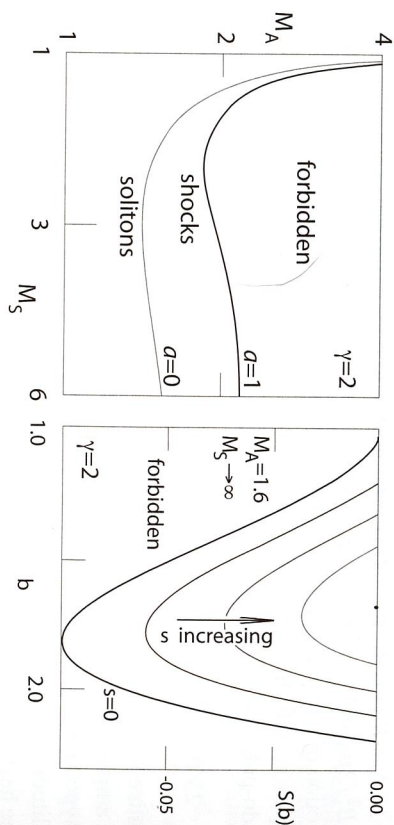


Figure 13.3: *Left:* The allowed regions in (M_A, M_S) -space for solitons and shocks depending on the dissipation coefficient a . Subcritical shocks exist only in the narrow domain between the two curves for $0 < a < 1$. *Right:* The shape of the Sagdeev pseudo-potential, $S(b)$, for $M_A = 1.6$, $M_S \rightarrow \infty$ as function of the entropy density s . For $s = 0$, corresponding to $a = 0$, the Sagdeev pseudo-potential has its largest excursion into the negative domain. For this case, solitons exist throughout the entire region inside the curve. With increasing s the domain shrinks, and no soliton solutions exist anymore, being replaced by shock solutions. A shock starts at one of those curves and wanders upward in the diagram until it reaches the maximum entropy point on the $S = 0$ axis (black dot).

in ∇_x) term describes the higher-order dispersion. One may recognise this equation as the shock model equation Eq. (13.5) if taking the stationary case and integrating one time with respect to space x . It then leads to the definition of the Sagdeev pseudo-potential.

With the example of the above equation one can discuss the effects of dissipation and dispersion. If diffusion dominates, entropy is produced, and steeping ceases, a ramp evolves, and the wave turns into a shock. If dispersion dominates, the shorter wavelength waves run away and a stationary wave packet of finite size is produced which is not a shock, but can, under certain circumstances, also evolve into a shock if the wavelength of the packet shrinks further until it reaches the dissipation scale, L_d . In subcritical shocks this effect ultimately takes place.

Hence the question arises as to how the required anomalous dissipation is generated? We do not go into detail of this process as it is strongly nonlinear. The idea is that particles – mostly electrons – are scattered in the self-excited waves, which becomes equivalent to a braking of their speed. This is just the effect of friction, resistance and dissipation, because it is the electrons which carry the current. The anomalously produced collision frequency is given by the celebrated Sagdeev formula:

$$V_a \simeq (W_{sat}/nk_B T_e) \omega_{pe}, \quad (13.8)$$

where W_{sat} is the saturation amplitude of the waves, mostly ion-acoustic waves excited by the current, which replaces the thermal fluctuation level when the ion-acoustic waves become unstable in the shock.

The dissipation depends crucially on the particular wave spectrum, W_k . There is a large number of possibilities of which kind of waves are excited by the electric current in the shock front. In subcritical shocks, identification of the waves is necessary, while in supercritical shocks it is not of primary importance for the shock dynamics. Candidates for unstable waves are the two-stream instability, which becomes unstable at current drifts $V_{||} > v_e$, i.e., at very high current speeds, preferentially in supercritical shocks. In subcritical shocks it is mostly the ion-acoustic instability which is unstable at thermal speeds $v_e > V_{||} > c_{ia}$, when the current drift speed exceeds the ion acoustic velocity c_{ia} , the latter causing an anomalous collision frequency $V_a \simeq 0.01 (V_{||}/c_{ia}) (T_e/T_i) \omega_{pi}$, being favoured by high electron temperatures, $T_e \gg T_i$.

In subcritical shocks two other waves may be more important: the lower-hybrid-drift instability and the modified-two-stream instability. The former arises when the scale of width of the shock front is comparable to the ion inertial length, $\Delta_{sh} \sim \lambda_i$. The latter can be excited when the currents flow perpendicular to the magnetic field, as is the case for the electron current in the shock ramp. Both instabilities have much lower thresholds than the two-stream and ion-acoustic instabilities. They yield comparably large anomalous collision frequencies, $V_a \sim \omega_{hi}$, of the order of the lower-hybrid frequency, $\omega_{hi} \simeq \sqrt{m_e/m_i} \omega_{ce}$, being candidates for the required dissipation in subcritical shocks.

Cross-shock Potential and Dissipation Scale

Subcritical shocks do not reflect ions. All upstream ions pass the shock. However, the shock ramp, being of the order of the ion inertial length, $\Delta_{sh} \sim \lambda_i$, allows for the ions to be non-magnetised while the electrons are tied to the magnetic field. As a consequence, the shock ramp contains a finite electric potential, U , which retards the ions, but is not large enough to stop their motion and to reflect them. Neglecting any upstream thermal spread of the ions which move at upstream bulk velocity V_1 , the ion speed, v_x , across the shock is therefore given by

$$v_x(x) = [V_1^2 - 2eU(x)/m_i]^{1/2}, \quad n(x) = n_1 [V_1/v_x(x)], \quad (13.9)$$

independent of how complicated the real motion of the ions would be in crossing the ramp. Pressure balance requires $m_i n v_x^2 + P + B^2/2\mu_0 = \text{const}$, ($P \equiv P_i + P_e$). Substituting for v_x yields with $\bar{U} \equiv 2eU/m_i V_1^2$ and upstream flow ram pressure $P_{\text{ram}} = \frac{1}{2} m_i n_1 V_1^2$,

$$\frac{n(x)}{n_1} = \frac{1}{[1 - \bar{U}(x)]^{1/2}} \left\{ 1 + \frac{3}{4} \frac{\beta_i}{M_A^2} \frac{\bar{U}(x)}{[1 - \bar{U}(x)]^2} \right\}, \quad \frac{P_i(x)}{P_{\text{ram}}} = \frac{\beta_i/M_A^2}{[1 - \bar{U}(x)]^{3/2}}, \quad (13.10)$$

as an implicit expression for the shock potential, $\bar{U}(x)$, at position x in the shock ramp. At the top of the ramp the ions have velocity $V_R(x_R)/V_1 = (1 - \bar{U}_{\text{tot}})^{1/2}$, where \bar{U}_{tot} is the total normalised ramp potential drop. The corresponding velocity is less than the upstream speed but does not coincide with the downstream velocity, V_2 , determined

from the Rankine–Hugoniot relations. The difference, $V_R - V_2$, gives the downstream gyration speed and the downstream ion temperature, $T_2 \sim m_i (V_R - V_2)^2/2$. The potential drop obeys the condition $U < 1 - V_2^2/V_1^2$. Ion deceleration in the ramp is solely due to the shock potential.

The dissipation length of the shock transition is obtained from shock width, Δ_{rms} , and the induction equation

$$\partial \mathbf{B} / \partial t = \nabla \times \mathbf{V} \times \mathbf{B} - (\eta_{an} / \mu_0) \nabla^2 \mathbf{B}. \quad (13.11)$$

Dissipation is active only during the convection time, $\tau_{sh} = \Delta_{sh} / V_1$, yielding the dissipation time, $\tau_d = L_d^2 \mu_0 \eta_{an}^{-1} < \tau_{sh}$, to be shorter than the crossing time. Alternatively, the ‘dissipation scale’, $L_d < \Delta_{sh}$, is shorter than the shock width. Dimensionally, we obtain for the dissipation scale

$$L_d^2 \lesssim (\eta_{an} / \mu_0) (\Delta_{sh} / V_1), \quad (13.12)$$

which when inserting for the anomalous resistivity yields a condition on the anomalous collision frequency generated in the shock transition,

$$v_{an} \gtrsim \alpha \left(\frac{V_1}{\lambda_e} \right) \left(\frac{\Delta_{sh}}{\lambda_e} \right), \quad \text{or equivalently} \quad v_{an} \tau_{sh} \gtrsim \alpha \left(\frac{\Delta_{sh}}{\lambda_e} \right)^2, \quad (13.13)$$

where $\alpha \lesssim 1$ is a numerical factor of proportionality. For anomalous dissipation to be sufficiently large to sustain the shock, the second version of this condition suggests that the ratio of transition-time to collision-time must thus be larger than a fraction, α , of the square of the shock width measured in electron inertial lengths.

As an example, let us assume that the shock width is $\Delta_{sh} = 1000$ km, like in the bow shock. Then, for a plasma density of $n \sim 5 \times 10^6 \text{ m}^{-3}$ and a subcritical flow velocity of $V_1 = 100$ km/s, the anomalous collision frequency should be larger than $v_{an} > 10^4 \alpha \text{ Hz}$, which is of similar order as the electron plasma frequency, $f_{pe} \sim 20$ kHz. Since such high anomalous collision frequencies are unrealistic, one must require $\alpha \sim 0.1$, corresponding to a substantially narrower dissipation scale, $L_d \sim 0.3 \Delta_{sh}$, or, correspondingly, narrower current sheets inside the shock transition.

13.2 Quasi-perpendicular Shocks

Subcritical shocks probably exist in multitude in the near-Earth space plasma. However, in most cases their Mach numbers are marginally larger than $M = 1$, such that they represent just one component of the general turbulence, as long as they are not of very large amplitude. On the other hand, super-critical shocks are relatively rare. When they occur, however, they are accompanied by large and sometimes violent effects. One of them, Earth’s bow shock wave, is permanently present in near-Earth space, allowing for a monitoring and investigation of super-critical shock properties.

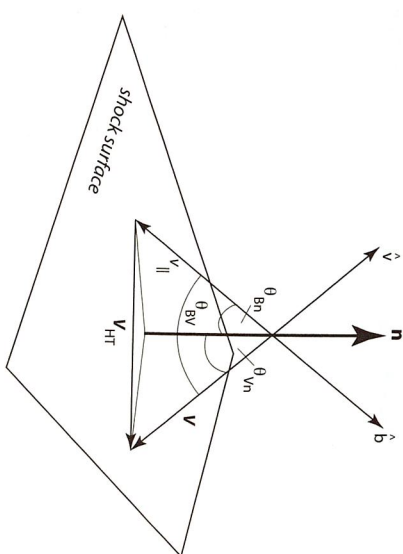


Figure 13.4: The shock coordinate system showing the shock normal \mathbf{n} , velocity and magnetic field directions \hat{v}, \hat{b} , the three angles $\Theta_{bn}, \Theta_{v/n}, \Theta_{bv}$ between \hat{b} and \mathbf{n} , velocity \mathbf{V} and \mathbf{n} , and velocity \mathbf{V} and \hat{b} , respectively. The velocity \mathbf{V}_{HT} in the shock plane is the de Hoffmann–Teller velocity.

The first of these properties is that super-critical shocks do not form one class but decay into two families of shocks, depending on the angle between the shock normal and the direction of the upstream magnetic field, the so-called *shock normal angle*, Θ_{bn} . Referring to this angle it is customary to distinguish between quasi-perpendicular and quasi-parallel shocks whether $\Theta_{bn} > \frac{1}{4}\pi$ or $\Theta_{bn} < \frac{1}{4}\pi$, respectively. Such a distinction looks artificial though reasonable. It turns out, however, that when considering the particle dynamics during an encounter with a super-critical shock, this distinction is a natural condition on two families of shocks exhibiting completely different behaviour.

13.2.1 Dynamics of Particle Reflection

Figure 13.4 shows the coordinate frame used at the planar shock, which is assumed to be super-critical with shock normal \mathbf{n} , magnetic and velocity unit vectors \hat{b}, \hat{v} , respectively. Shown are the angles $\Theta_{bn}, \Theta_{v/n}, \Theta_{bv}$. The velocity vector, \mathbf{V}_{HT} , is the de Hoffmann–Teller velocity which lies in the shock plane and is defined in such a way that in the coordinate system moving along the shock plane with velocity \mathbf{V}_{HT} the plasma flow is along the magnetic field, $\mathbf{V} - \mathbf{V}_{HT} = -v_{\parallel} \hat{b}$. The guiding centres of the particles in this frame move all along the magnetic field.

For the latter reason it is convenient to consider the motion of particles in the de Hoffmann–Teller frame. Hence, the velocity vector has the two components:

$$v_{\parallel} = V (\cos \Theta_{v/n} / \cos \Theta_{bn}), \quad (13.14)$$

$$\mathbf{V}_{HT} = V [-\hat{v} + \hat{b} \cos \Theta_{v/n} / \cos \Theta_{bn}] \equiv (\mathbf{n} \times \mathbf{V} \times \mathbf{B}) / \mathbf{n} \cdot \mathbf{B}. \quad (13.15)$$

Because B_n and the tangential electric field are both continuous, the de Hoffmann–Teller velocity is the same to both sides of the shock ramp. There is no induction

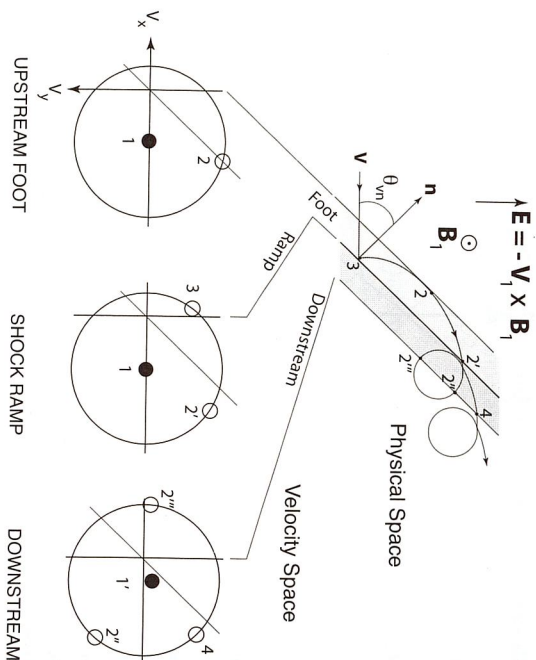


Figure 13.5: *Top:* Reflected ion orbits in the foot of a quasi-perpendicular shock in real space. The ion impacts under an instantaneous angle θ_n , is reflected from the infinitely thin shock, performs a further partial gyration in the upstream field \mathbf{B}_1 , where it is exposed to the upstream convection electric field $\mathbf{E} = -\mathbf{V}_1 \times \mathbf{B}_1$, in which it is accelerated as is seen from the non-circular section of its orbit in the shock foot. It hits the shock ramp a second time, now at energy high enough to overcome the shock potential, passing the ramp and arriving in the compressed downstream magnetic field behind the shock, where it performs gyrations of reduced gyroradius. *Bottom:* The ion distribution function mapped into velocity space v_x, v_y for the indicated regions in real space, upstream in the foot, at the ramp, and downstream of the shock ramp. Upstream the distribution consists of the incoming dense plasma flow (population 1, dark circle at $v_y = 0$) and the reflected distribution 2 at large negative v_y . At the ramp, in addition to the incoming flow 1 and the accelerated distribution 2, there is the newly reflected distribution 3. Behind the ramp in the downstream region the inflow is decelerated 1' and slightly deflected toward non-zero v_y , and the energised passing ions exhibit gyration motions in different instantaneous phases, two of them (2', 4) directed downstream, one of them (2'') directed upstream.

electric field, $\mathbf{E} = -\mathbf{n} \times \mathbf{V} \times \mathbf{B}$. The remaining problem is two-dimensional (see the coplanarity theorem which holds strictly in this purely kinematic case). The particle velocity is described by the motion along \hat{b} plus the gyro-motion in the plane perpendicular to \hat{b} :

$$\mathbf{v}(t) = v_{\parallel} \hat{b} + v_{\perp} [\hat{x} \cos(\omega_{ci} t + \phi_0) \mp \hat{y} \sin(\omega_{ci} t + \phi_0)]. \quad (13.16)$$

The unit vectors, \hat{x}, \hat{y} , point along the orthogonal coordinates in the gyration plane of the ion, the phase, ϕ_0 , accounts for the initial gyro-phase of the ion, and \pm accounts for the direction of the upstream magnetic field being parallel (+) or antiparallel to \hat{b} . In specular reflection the velocity component along \mathbf{n} is reversed, and (for cold ions) becomes $\mathbf{v}' = -v_{\parallel} \hat{b} + 2v_{\parallel} \cos \Theta_{Bn} \hat{n}$, which (with $\phi_0 = 0$) yields

$$v'_{\parallel}/V = [\cos \Theta_{Bn} / \cos \Theta_{Bn}] (2 \cos^2 \Theta_{Bn} - 1), \quad (13.17)$$

$$v_{\perp}/V = 2 \sin \Theta_{Bn} \cos \Theta_{Bn}. \quad (13.18)$$

A reflected particle returns to the shock when the upstream component of the velocity $v_x = 0$, which for $\phi_0 = 0$ yields

$$\mathbf{x}'(t) = v'_{\parallel} t \hat{b} + (v_{\perp} / \omega_{ci}) \{ (\sin \omega_{ci} t) \hat{x} \pm (\cos \omega_{ci} t - 1) \hat{y} \}. \quad (13.19)$$

After scalar multiplication of this expression with \mathbf{n} , the ion displacement normal to the shock in upstream direction becomes

$$\mathbf{x}'_{\mathbf{n}}(t^*) = v'_{\parallel} t^* \cos \Theta_{Bn} + (v_{\perp} / \omega_{ci}) \sin \Theta_{Bn} \sin \omega_{ci} t^* = 0. \quad (13.20)$$

It vanishes at time t^* , when the ion re-encounters the shock with normal velocity, $v_n(t^*) = v'_{\parallel} \cos \Theta_{Bn} + v_{\perp} \sin \Theta_{Bn} \cos \omega_{ci} t^*$. Setting this to zero, one obtains for the maximum displacement time

$$\omega_{ci} t_m^* = \cos^{-1} [(1 - 2 \cos^2 \Theta_{Bn}) / 2 \sin^2 \Theta_{Bn}], \quad (13.21)$$

which must be inserted in $\mathbf{x}_{\mathbf{n}}$, yielding for the distance a reflected ion with gyroradius $r_{ci} = V / \omega_{ci}$ can reach in upstream direction

$$\Delta x_n = r_{ci} \cos \Theta_{Bn} [\omega_{ci} t_m^* (2 \cos^2 \Theta_{Bn} - 1) + 2 \sin^2 \Theta_{Bn} \sin \omega_{ci} t_m^*]. \quad (13.22)$$

This distance, for a perpendicular shock $\Theta_{Bn} = 90^\circ$, is

$$\Delta x_n \simeq 0.7 r_{ci} \cos \Theta_{Bn}, \quad (13.23)$$

which is less than an ion gyroradius. Note that this distance depends strongly on the angle the velocity makes with the normal of the shock, and on the shock normal angle.

The important conclusion is drawn from consideration of the argument of \cos^{-1} in the expression (13.21) for $\omega_{ci} t_m^*$, which exceeds unity for $\Theta_{Bn} \leq 45^\circ$. Hence, there are no solutions for such angles.

Reflected ions return to the shock only when the magnetic field makes an angle with the shock normal larger $\Theta_{Bn} > 45^\circ$. For less inclined shock normal angles the reflected ions escape along the magnetic field upstream of the shock and do not return. This sharp distinction between shock normal angles, $\Theta_{Bn} < 45^\circ$ and $\Theta_{Bn} > 45^\circ$, thus provides the clear natural discrimination between quasi-perpendicular and quasi-parallel shocks we were looking for.

Of course, this sharp distinction holds strictly just under the simplifying assumption of specular reflection made earlier.

13.2.2 Shock Foot and Reformation

The previous section showed that super-critical shocks necessarily reflect particles. This has been accounted for by inverting the normal velocity component of an incoming particle at the shock. The mechanism of reflection has not yet been clarified. It remains an active field of shock research. Clearly the cross shock electric field is involved. However, the mechanism is more complicated because numerical simulations show that the incoming particles experience some violent retardation, which a simple electric field can hardly explain. We do not go into detail of the processes involved here.

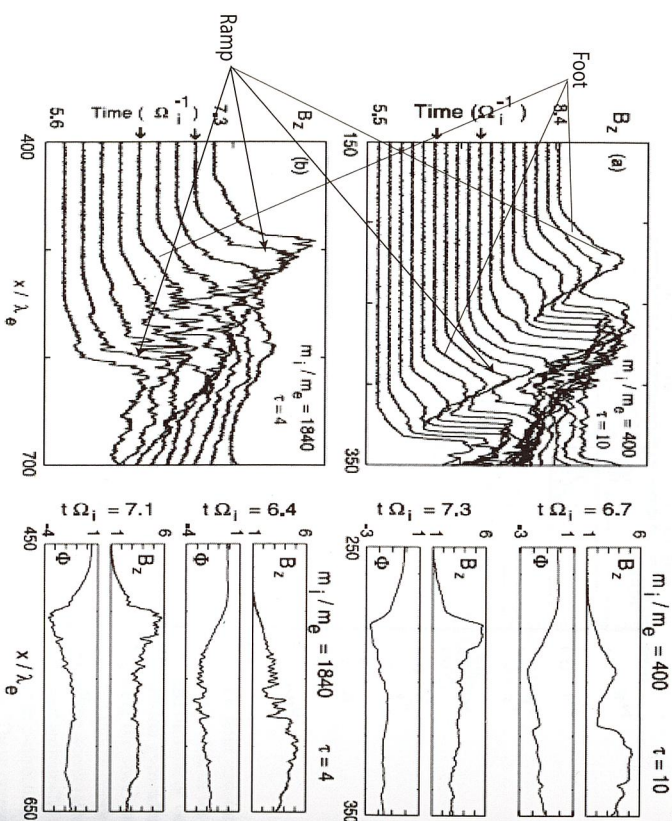


Figure 13.8: *Left:* 1D-PIC simulations of quasi-perpendicular, $\Theta_{Bn} = 87^\circ$, shock reformation (mass ratios $m_i/m_e = 400$ and 1840). Time is in ω_{pe}^{-1} , space in λ_e and small $\tau = \omega_{pe}^2/\omega_{ce}^2$. Higher mass ratios show strong time evolution. Reformation is due to evolution of shock feet. *Right:* Spatial profiles at two time sections (see arrows on the left). The higher mass ratio shows structure in B_z and shock potential Φ . Potential drops appear in foot and ramp [courtesy of The American Geophysical Union].

in the density of energetic ions, N_i , and magnetic field, B , for both spacecraft. The electrons also react to the presence of the foot which is, however, a secondary effect due to instability of the foot current. We will briefly discuss it later when presenting numerical simulations.

Quasi-perpendicular Shock Reformation

An important question arises when asking whether the super-critical shock can remain in a stationary state when the foot forms. Imagine that ions will be reflected from the shock transition, pass into the solar wind, gyrate, become accelerated, increase their velocity along the shock ramp, and cause a strong current flowing along the ramp. If there would be no flow-electric field upstream of the shock, the ions would just gyrate and return into the shock, forming an ion layer and weak current simply because they have no faster gyration than the upstream solar wind ions.

However, when accelerated, they firstly extract energy from the solar wind which will be retarded in the foot region, and secondly they amplify the foot current. The

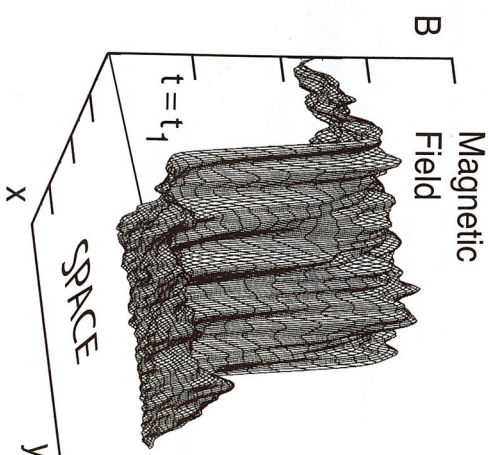


Figure 13.9: Ripples evolving on the shock ramp plane found in two-dimensional numerical simulations of quasi-perpendicular shocks. The ripples deform the shock along the shock plane during reformation. The figure shows the magnetic field amplitude at one particular simulation time as a function of the two space coordinates, x, y , across and along the shock. These simulations use a low mass ratio, but it is not expected that at realistic mass ratios no rippling occurs.

magnetic field of this foot current, which is a current sheet, is strongest at the outer edge of the foot, where it grows during amplification. This implies that the solar wind running into the shock already encounters a magnetic ramp located at the upstream edge of the foot and starts compressing it. This again leads to its growth and to reflection of ions at its place, which now form a new foot along the outer edge of the foot. At the same time an already retarded solar wind arrives at the shock, which consequently weakens, loses its function, and disappears, while a new shock forms at the outer edge of its foot.

This process is repeated roughly periodically. A supercritical quasi-perpendicular shock which builds up a foot consisting of reflected ions thus cannot be stable. It continuously reforms itself as a consequence of foot formation, each time when reformation takes place jumping ahead by one reflected ion gyroradius.

Since, in the solar wind frame, the shock moves against the solar wind, it turns out that this motion is not continuous, but consists of a sequence of periodic jumps of the shock front. In the stationary frame of the Earth one instead observes a motion of the shock, back and forth with the period of reformation and a scale comparable to the reflected ion gyroradius. Moreover, since this happens locally at the shock, the shock surface must exhibit a rippled structure, as seen in Fig. 13.9, identifying the shock as a non-stationary phenomenon.

This reformation is shown in one-dimensional numerical full-particle simulations in Fig. 13.8. Corresponding two-dimensional simulations confirm the irregular structure of the real quasi-perpendicular shock surface, which is far from being a plane, as

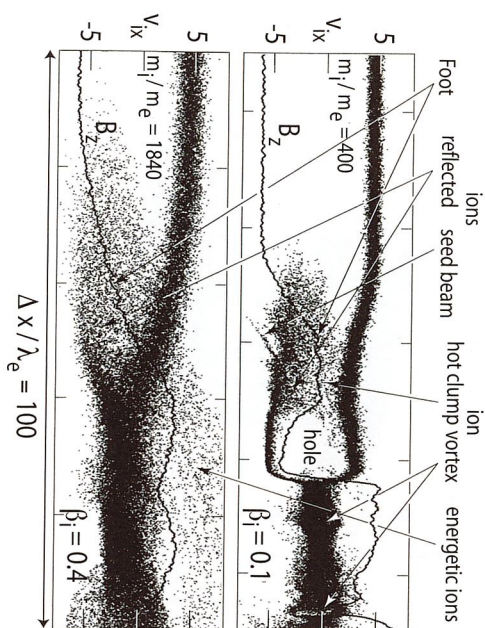


Figure 13.10: Ion phase space for $\beta_e = 0.2$ but different mass ratios and β_i [after] at same Mach number. *Top:* $\beta_i = 0.1$ simulation. A low-field hot clump-vortex is formed which scatters reflected and upstream ions. Reformation cycles appear in the downstream distribution as ion vortices (holes). *Bottom:* Realistic mass ratio but $\beta_i = 0.4$. Hot foot ions smear out the gap between inflowing and reflected ion beams. Large numbers of diffuse energetic ions appear in this case [courtesy of The American Geophysical Union].

was assumed in the simple Rankine–Hugoniot fluid approach in plasma magnetohydrodynamics in Chapter 8.

13.2.3 Particle Dynamics

Ion Dynamics in Quasi-perpendicular Shocks

Figure 13.8 gives a clear idea of the behaviour of ions in the reformation process. The corresponding ion phase space plots are shown in Fig. 13.10 for the two mass ratios, $m_i/m_e = 400$ (top) and 1840 (bottom), respectively. Both plots show just the enlarged shock foot transition region over the same scale of $100c/\omega_{pe}$ for the same $\beta_e = 0.2$, which has been kept constant in both simulations, while the β_i has been changed. Only the normal component of the ion velocity is shown for the nearly perpendicular supercritical shock. In both plots the magnetic field, B_z , is drawn as a thin continuous line showing the magnetic shock profile over the spatial distance, Δx .

In the low-mass-ratio low- β_i simulations the cold dense ion inflow at velocity $v_{ix} \sim 5$ (in units of the upstream Alfvén velocity) is retarded to nearly $M \approx 1$ when entering the foot. This retardation is due to its interaction with the intense but cold (narrow in velocity space) reflected ion beam, which is seen as the narrow negative v_{ix} -velocity beam originating from the shock ramp.

This reflected ion beam needs a certain distance to interact with the upstream plasma inflow. This distance is the growth-length of the beam-beam excited waves.

At this location the reflected ions are scattered into a hot ion clump in addition to being turned around by gyration. Both effects cause a reduction in velocity, v_{ix} , of the reflected ions which, being accelerated in the convection electric field, turn to flow in y direction, causing the magnetic bump that develops in this region of the foot. In the (v_x, x) -plane the reflected ions close with the upstream flow into an hot ion ring distribution (vortex) just in front of the ramp of which the hot ion clump that brakes the inflow is the upstream boundary.

Behind the ramp, which is the point of bifurcation of the ion distribution, i.e., the location where the reflection is at work, a broad hot ion distribution arises, which at some locations shows rudimentary remains of ion vortices from former reformation cycles. Their magnetic signatures are the dips seen in the magnetic field.

The next reformation cycle can be expected to completely close the ion vortex in the foot and to transform the ramp from its current position to the position of the foot. The first sign of this process is already seen in the foot-ion distribution, which shows the birth of a faint new reflected ion beam at high negative speeds. This beam is not participating in the formation of the ring but serves as the seed of the newly reflected population.

A similar behaviour is found in realistic mass-ratio simulations as long as β_i is small (this is obvious from the realistic mass-ratio magnetic field shown in Fig. 13.8). The shock in this case also undergoes reformations for realistic mass ratios. In other words, as long as the plasma is relatively cool or the magnetic field strong the real shocks found in nature should develop feet, which at later times quasi-periodically become the shock ramp.

This changes when β_i increases, the plasma is either hot or the magnetic field weak, as is suggested by the lower panel in Fig. 13.10. There, a realistic mass ratio has been assumed, but $\beta_i = 0.4$. No reformation is observed, at least not for the simulation time. Instead, the shock develops a very long foot region that extends upstream about twice as far as for low- β_i . The high ion temperature smears out the reflected ion population over the entire gap region between upstream and reflected beam regions, and no current vortex or new magnetic ramp can develop. This implies that the foot remains smooth and does not evolve into a secondary ramp.

Reformation in two dimensions will thus be suppressed only when the thermal speed, v_i , of the ions is large enough to bridge the gap between the reflected and incoming ion beams, i.e., large enough to fill the hole in phase space between them by scattering the ions in their self-generated waves by ion-ion beam instability. Semi-empirically, based on the simulations, one can establish a condition for shock reformation as

$$v_i < \alpha V_{A1}, \quad 1.5 < \alpha < 2, \quad (13.24)$$

when taking into account that the normal speed of incoming ions is specularly turned negative. Since this is never exactly the case, the coefficient, α , will roughly be in the indicated interval. This condition for reformation to occur can also be written as

$$\beta_i < \alpha M_A^2, \quad (13.25)$$

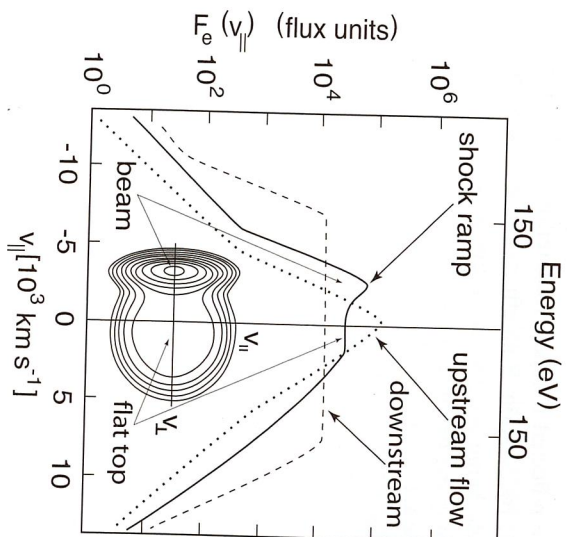


Figure 13.11: Successive reduced parallel electron distributions, $F_e(v_{||})$, in the supercritical Earth's bow shock. The transition from the Maxwellian-plus-halo upstream flow distribution through the shock ramp distribution to the shock downstream distribution is monitored. The shock ramp distribution is intermediate electron beam of velocity of a few 1000 km s^{-1} , which is sufficiently fast to excite electron plasma waves [courtesy of The American Geophysical Union].

where the Alfvénic Mach number is defined on V_{in} . The larger the Mach number the less suppression of reformation takes place.

Electron Dynamics in Quasi-perpendicular Shocks

Observations *in situ* the quasi-perpendicular Earth's bow shock wave (plotted in Fig. 13.11) indicate that electrons are strongly heated when crossing the shock from upstream to downstream. Their reduced (field-parallel) distribution changes from Maxwellian to hot flat-top type with the intermediate distribution observed in the shock ramp, showing signs of a shock-reflected electron beam. This heating and electron reflection is typical for supercritical shocks.

In the foot region of a perpendicular highly supercritical shock the velocity differences between reflected ions and electrons from the upstream plasma inflow is large enough for the excitation of the Buneman two-stream instability and heating of the electrons, which contributes to shock formation. Full particle PIC simulations in strictly perpendicular shocks for small mass ratio of $m_i/m_e = 20$, $\beta_i = \beta_e = 0.15$, and Alfvénic Mach numbers $3.4 \leq M_A \leq 10.5$, discovered that the Buneman two-stream instability can indeed be at work.

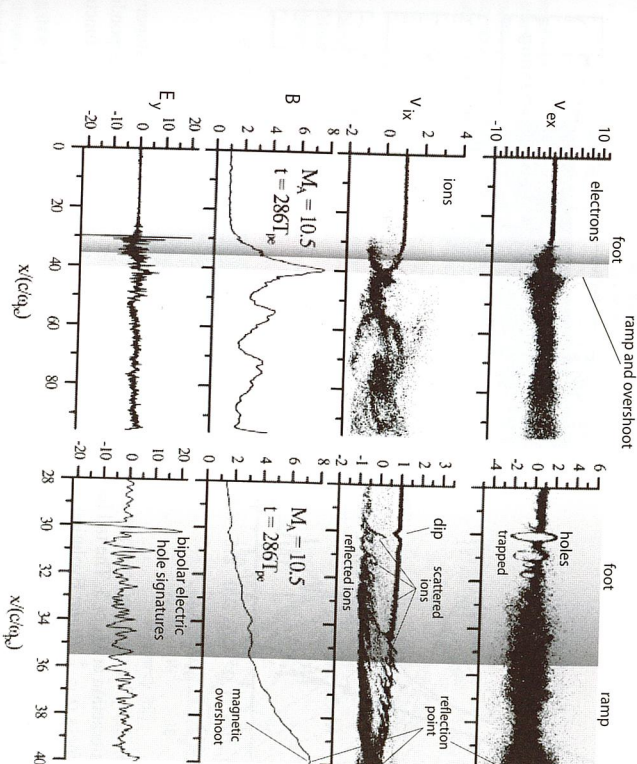


Figure 13.12: Electron dynamics in 1D-PIC simulations for $m_i/m_e = 20$, $M_A = 10.5$, $\Theta_{Bn} = 90^\circ$ for quasi-perpendicular shocks. *Left:* Electron/ion phase space, magnetic field, electric field. Second panel: Ion reflection and foot formation. Bottom: Foot-electron heating in large electric field amplitudes. *Right:* Expanded view of shaded regions. Electron heating related to hole formation. Three Buneman holes form potential (lowest panel) in the overshoot. Ion distribution is highly structured due to interaction with many small-scale electron holes.

Figure 13.12 shows the results in expanded view on the right in electron phase space. Development of electron holes generated by the Buneman two-stream instability is seen. The electrostatic field, E_y , in the bottom panel shows the bipolar electric field structure caused by the holes with zero mean. E_y assumes large values in the holes, the behaviour expected for solitons and BGK modes trapping and heating electrons and accelerating, passing electrons to high speeds, happening in the simulations near the shock. Three such holes are completely resolved, with decreasing amplitude closer to the shock ramp. They contain a small number of trapped electrons over a wide range of speeds, which on the gross scale in the left panel fakes the high temperature of the electrons. In addition, the electron velocity shows two accelerated populations, one with positive velocity about 2–3 times the initial electron speed, the other reflected component with velocity almost as large as the positive component but in the opposite direction, suggesting that the electron current in the holes is almost compensated by the electron distribution.

The magnetic signature confirms that the reflection of the main incoming ion beam takes place at the location of the magnetic overshoot and not in the shock ramp in the

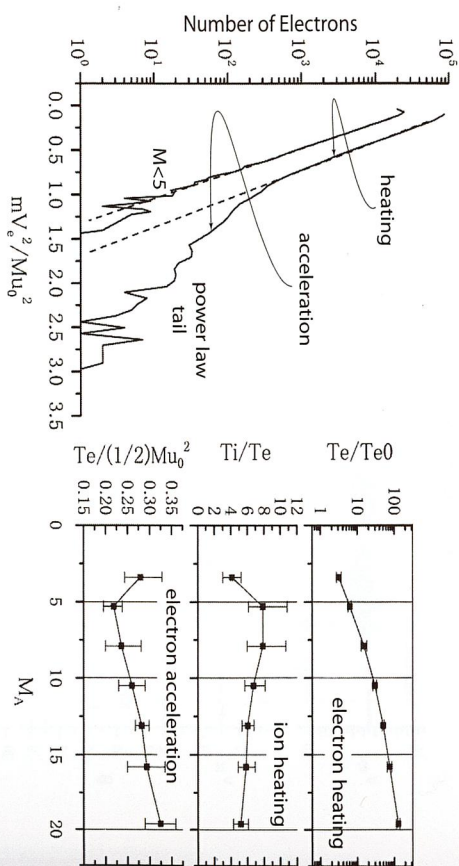


Figure 13.13: Left: Heating and energetic tail formation in shock-electron distribution from Buneman electron hole interaction at $M_A > 5$. The tail has power law shape $F(\varepsilon) \propto \varepsilon^{-\alpha}$, with $\alpha \approx 1.7$, corresponding to marginal flatness $\alpha = \frac{3}{2}$. Right: Evolution of average temperatures electron temperature ratio as function of M_A . All quantities are in computational units.

strictly perpendicular supercritical shock. The actual ramp region is narrow. Its width is of the order of

$$\Delta \sim (1 - 2)c / \omega_{pe}. \quad (13.26)$$

An extended electron tail is hereby generated on the electron distribution (Fig. 13.13 on its left shows the evolution of the tail in a log-lin representation). On a log-log scale the tail has a power law slope

$$F(\varepsilon) \propto \varepsilon^{-\alpha}, \quad (13.27)$$

notably with power $\alpha \approx 1.7$, close to the marginally flattest power, $\alpha = \frac{3}{2}$, below that an infinitely extended power law energy distribution cannot exist. The effect does not occur for small Mach numbers, too small for the Buneman two-stream instability to be excited. However, once excited, the heating increases strongly with M_A . Over the range $5 < M_A < 20$, the increase in electron temperature (electron energy in the tail of the distribution) is a factor of 40–50, which demonstrates the strong non-collisional but anomalous transfer of flow energy into electron energy via the two-stream instability.

Recently, the Polar satellite, when crossing the quasi-perpendicular Earth's Bow Shock, provided *in situ* measurements of very strong localised electric fields that exist on scales $\lesssim \lambda_e = c/\omega_{pe}$ and reach values of $\lesssim 100 \text{ mV m}^{-1}$ parallel and $\lesssim 600 \text{ mV m}^{-1}$ perpendicular to the magnetic field. These fields are related to the electron dynamics in the shock ramp. Presumably they play a substantial role in quasi-perpendicular shock dynamics.

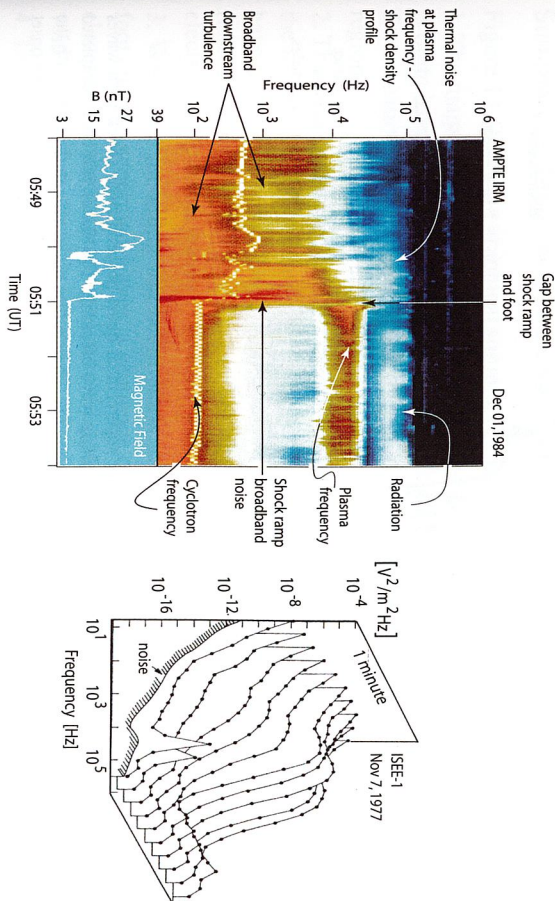


Figure 13.14: Electric wave spectra measured during spacecraft crossings of shocks in space. Left: An outbound bow shock transition by Ampe. The top panel is the dynamic spectrogram of power spectral energy density showing the intense low and medium frequency turbulence in the magnetosheath downstream of the shock, the violent shock transition with strong broad-band wave amplification, and the solar wind low frequency ion-acoustic waves, separated in frequency from the intense Langmuir waves at solar wind plasma frequency caused by the field-aligned electron beam emanating from along the electron foreshock boundary. The weak band at twice the plasma frequency is the electromagnetic radiation. The lower left panel shows the change in the magnetic field along the orbit of the spacecraft. Right: A sequence of shock electric spectra during another (this time inbound) crossing by Ise-1 of an interplanetary shock. Single spectra are shown exhibiting the dramatic increase of the low frequency wave power when the spacecraft approaches and crosses over the shock. Behind the shock the power remains high but lower than in the transition region. The bump around a few 100 Hz is the most interesting from the point of view of instability. These waves are excited by electron-ion instabilities, discussed in the next section. The sharp peak at 60 kHz in the solar wind is the electron plasma frequency excited by the foreshock boundary electron beam.

13.2.4 Waves

Plasma Waves and Radiation in Quasi-perpendicular Shocks

Figure 13.14 on its left shows six minutes of electric wave field spectra detected during an Ampe spacecraft crossing of Earth's bow shock. The spacecraft approaches the shock from the magnetosheath, downstream of the bow shock, seeing the strongly turbulent magnetosheath plasma with the irregular broad-band wave spectra followed by the shock crossing, which is indicated by the strong intensification of the low and medium frequency waves. In the upstream plasma it records the general solar wind low frequency ion-acoustic turbulence at frequency $\lesssim 1 \text{ kHz}$. Centred at $\approx 31 \text{ kHz}$, the highly enhanced wave intensity shows the presence of intense electron plasma waves with frequency $\omega \simeq \omega_{pe}$. They are generated by the electron beam which has been

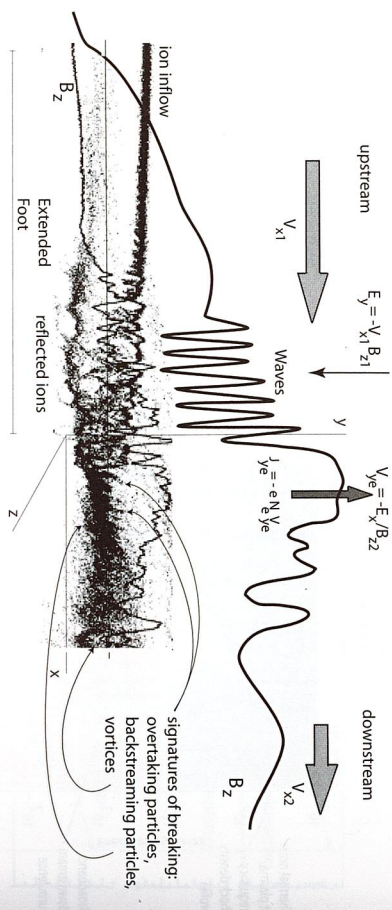


Figure 13.15: Schematic of the profile of a highly supercritical quasi-perpendicular shock with waves just before shock reformation and signatures of beginning wave breaking. The sketch has been completed with a copy of the ion phase space from simulations showing the structure of the ions in the ramp with the signatures of overtaking ions and backstreaming ions as well as ion vortices, all an indication of the onset of breaking in the particle component.

accelerated along the electron foreshock boundary and reaches the spacecraft along the foreshock boundary magnetic field line which connects the spacecraft with the shock. These emissions are highly irregularly in intensity, bandwidth and time. Some signatures of these highly fluctuating waves are also seen near 18 kHz, and due to nonlinear effects occasionally down to 1 kHz, as, for instance, at 2250:30 UT. The electron plasma waves disappear when approaching the shock at 0553 UT.

The sequence of spectra at the right taken at another crossing, this time of a traveling interplanetary reverse shock in the solar wind, shows the sharp plasma wave peak near 60 kHz in the first few spectra and the gradual evolution of the broad-band noise peaking around 0.5 kHz, related to the Buneman instability and also to a Modified Two-Stream instability of a current perpendicular to the magnetic field, similar to the Buneman instability. It also indicates the presence of localised electron holes in the shock, as we discussed earlier.

Radiation from the shock can be recognised upstream at higher frequencies in the left panel during bow shock crossing at about twice the electron plasma frequency. It is emitted as second harmonic radiation, $\omega \simeq 2\omega_{pe}$. It is produced by the foreshock-boundary electron beam-excited electron plasma waves in a narrow frequency band. The mechanisms of generating radiation in supercritical collisionless shocks are well known to be a three-wave 'collision' between three waves, two Langmuir waves, and the escaping free space electromagnetic wave, symbolically written as

$$L + L' \rightarrow T, \quad (13.28)$$

where L, L' are the two involved longitudinal waves and T is the radiated transverse wave.

Summary of Quasi-perpendicular Shock Properties

Figure 13.15 gives a graphical summary of the structure of quasi-perpendicular shocks.

1. The magnetic profile shows the extended shock foot which, close to the shock ramp, is quite irregular, being modulated by low frequency propagating waves. The ramp is the transition to a smoother shock overshoot profile and from there to the downstream region.
2. The ion phase space exhibits both the incoming and reflected ion beams. In the foot, the former is already retarded, showing the signatures of the slowed down ions, which have been scattered in the wave fields inside the foot, which have been excited by the reflected ions and the foot ion current through instabilities of low frequency mostly electrostatic plasma waves.
3. When the incoming ion beam starts interacting with the reflected beam and the foot current-generated waves, a sequence of phase-space structures is formed, which, closer to the shock ramp, evolve into large holes in ion phase space being practically void of ions, incoming or reflected.
4. The shock ramp is the location of the ultimate ion reflection and heating of the bulk distribution. Signatures of onset of wave breaking are seen in the overtaking particles. However, breaking seems not to take place, which is probably due to the environment of a shock of being deep, i.e., not bounded in any spatial direction.
5. The entire transition region, including the foot and downstream region, contains a diffuse hot energetic ion component that has been accelerated in the shock.
6. The plasma state just downstream of the shock is nothing but the collection of the old shock ramps, which have been left over from former shock-foot reformation cycles and, relative to the shock frame, move in the direction downstream of the shock.
7. The simulations show that, in more than one dimension, the shock front is far from being a plane surface. It exhibits a strong variability in time and space. Some of this variability can be explained as surface waves propagating along the shock front. These surface waves are mostly due to the quasi-periodic shock foot-reformation process described. Otherwise, they might also be driven or additionally amplified by the reflected foot-ion current-flow along the quasi-perpendicular shock surface similar to a Kelvin-Helmholtz instability.

13.3 Quasi-parallel Shocks

The surprisingly sharp division between quasi-parallel and quasi-parallel shocks inferred from the investigation of specular reflection has its no less surprising pendant in real space. It has, in fact, been observed as a permanent property of Earth's bow shock, which by the nature of its geometry is a curved shock.

Figure 13.16 summarises the observations in front of the concavely bent bow shock – as seen from Earth – for the special case of an interplanetary magnetic incli-

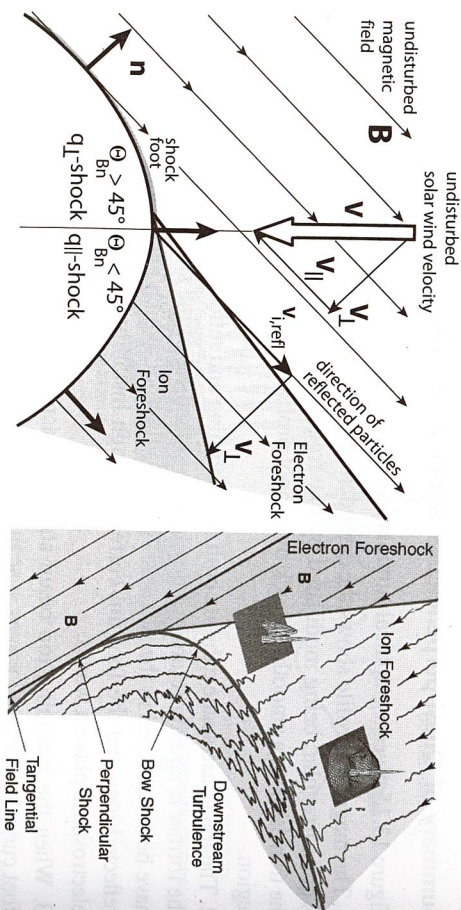


Figure 13.16: Two schematic views of the relation between a curved shock and its foreshock in dependence on the direction of the upstream magnetic field \mathbf{B} , shock-normal \mathbf{n} , and shock-normal angle Θ_{Bn} . *Left:* The special case when the magnetic field is inclined at 45° with respect to the symmetry axis of the shock. In this case the upper half of the shock becomes quasi-parallel ($\Theta_{Bn} < 45^\circ$), the lower half is quasi-perpendicular ($\Theta_{Bn} > 45^\circ$). The velocity of reflected particles is along the magnetic field. However, seeing the flow the field-line to which they are attached displaces with perpendicular velocity. This velocity shifts the foreshock boundary toward the shock, as shown for electrons (light shading) and ions (darker shading). The ion foreshock is closer to the shock because of the lower velocity of the ions than the electrons. For the electrons the displacement of the electron foreshock boundary is felt only at large distances from the shock. *Right:* The different velocity space ion distribution function (inserts) along the ion foreshock boundary and deep inside the ion foreshock. Also shown is the different character of the magnetic fields in the quasi-perpendicular and quasi-parallel shocks. Note also the quiet state of \mathbf{B} in the electron foreshock region.

nation angle of 45° against the Earth–Sun line in the ecliptic. In this figure, the bow shock is the hyperbolic curve in the lower part of the left panel and on the right in the right panel. At the 45° magnetic field inclination angle in the left panel, the field lines are tangential to the bow shock at its evening flank. Θ_{Bn} exceeds 45° up to about the nose of the bow shock. In this region the shock is quasi-perpendicular. Reflected particles form a foot, shown as the narrow shaded region in front of the bow shock which ends at the bow shock nose. The solar wind velocity, \mathbf{V} , splits into parallel and perpendicular parts, \mathbf{V}_\parallel , \mathbf{V}_\perp , as shown. Because of the direction of \mathbf{V}_\parallel in this region no particles escape along the magnetic field upstream of the quasi-perpendicular shock.

13.3.1 Foreshock

To the right of the bow shock nose on the left in Fig. 13.16 one has $\Theta_{Bn} > 45^\circ$. Here the reflected particles do escape upstream along \mathbf{B} , filling an extended region in front of the pre-noon side of the bow shock, called the foreshock.

13.3. Quasi-parallel Shocks

The boundary of the foreshock is thus a sharp line in space which is, however, more inclined against the solar wind magnetic field, because, during their upstream motion of escape, the particles are convected by the solar wind velocity together with their magnetic field line toward the bow shock. Since the electrons have higher velocity than the ions – we do not ask here, how they can escape from the bow shock and where they receive their high upstream directed velocities – the inclination angle of the electron foreshock is less than that of the ion foreshock, occupying a larger fraction of the upstream foreshock space than the ions. This double structure of the foreshock is what has been constantly observed at the bow shock and is a typical property of quasi-parallel super-critical shocks.

The foreshock of a supercritical shock is the most important structural property of quasi-parallel shocks. It forms a fan in front of the quasi-parallel shock which extends as far upstream as the fastest particles manage to travel along the magnetic field during the solar wind convection time.

These fastest particles occupy the flux tube at the edge of the foreshock. Upstream propagating electrons are first encountered at the edge of the electron foreshock, and upstream propagating ions are located at the edge of the ion foreshock. Here, at these spatially separated edges, the escaping particles form upward streaming beams of particles, which in the solar wind frame are more energetic than the corresponding solar wind particles. Roughly spoken, in the solar wind frame these particles propagate at twice the solar wind velocity because their downstream velocities have been inverted into upstream.

Together with the solar wind, they form a beam-beam plasma system, in which the solar wind is the hot background and the upstream beam is cold, because it consists solely of the fast particles along the edges of the foreshock. Thus, for the electrons, one has the classical configuration of a hot solar wind electron background distribution traversed by a colder fast electron beam, the configuration in which one expects strong excitation of Langmuir waves by the mechanism noted at the end of the last section. Similarly, the reflected ion at the ion-foreshock edge form a fast ion beam, interacting head-on with the solar wind ion stream.

The slower upstream particles, electrons and ions, feel the downstream convection stronger than the faster particles. As a consequence the solar wind convection flow sweeps them readily away from their own foreshock boundary into the centre of the foreshock. The foreshock is therefore filled with a broad population of particles of lesser energy and slower speed than those particles in the foreshock-edge beams. Moreover, these lower energy particles interact with the spectrum of waves present in the foreshock and become scattered in phase space. For these reasons they possess a broadened distribution function than the solar wind and the reflected beam. This is shown on the right in Fig. 13.16, where two measured ion-velocity space distributions are shown as insets in the ion foreshock.

The first inset belongs to the ion-foreshock ion beam distribution. The square plane is the (v_x, v_y) -velocity plane. The distributions are plotted as a number of particles in this plane. The sharp large peak in the centre of the plane is the solar wind ion distribution (drawn in the solar wind frame), which has very little spread due to the

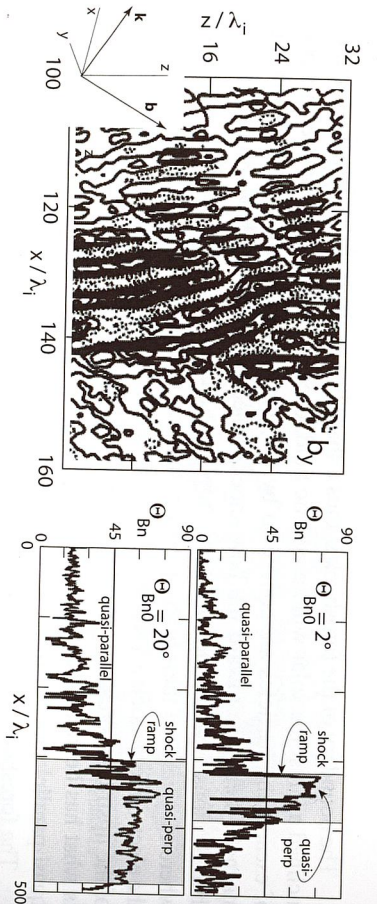


Figure 13.17: Two-dimensional simulations of the evolution of upstream waves. *Left:* Upstream waves in a super-critical quasi-parallel shock in the (y, z) -plane. Contour plot of the two (normalised to upstream magnetic field) components of magnetic fluctuations. Plane magnetic wave fronts inclined against the shock in direction x evolve for wavelengths $\sim 10\lambda_i$ in z and shorter in x . Near the shock the fronts turn parallel to the shock, producing a non-coplanar magnetic component $|b_y|$ of same order as $|b_z|$. The shock is not stable, exhibiting structure in z produced by the reflected upstream particles and waves. *Right:* Evolution two initial quasi-parallel shock-normal angles, $\Theta_{Bn0} = 2^\circ$ and $\Theta_{Bn0} = 20^\circ$, respectively. The horizontal line at 45° is the division between quasi-perpendicular and quasi-parallel shock normal angles. In both cases, Θ_{Bn} evolves from quasi-parallel direction into quasi-perpendicular direction. The shaded areas identify the locally quasi-perpendicular domains of the quasi-parallel shock as consequence of the upstream waves.

very low temperature (velocity spread) of the solar wind ions. Displaced from it, a smaller peak of slightly larger velocity spread is moving at upstream speeds (displaced into upward direction, i.e., solar direction from the solar wind peak). This is the warm reflected ion beam along the ion-foreshock edge. Its spread is larger than that of the observations; it fluctuates highly in space. For this reason one needs to average over a certain space interval in order to obtain a reliable measurement. In addition, however, the ion beam is unstable with respect to several kinds of low-frequency plasma waves, which scatter the ions in the beam causing a substantial spread of the beam in velocity.

The second inset is an example of an ion distribution much deeper in the ion foreshock. Still the undisturbed solar wind flow sticks out. But at the same time, the reflected ions, which have been swept into the foreshock, form a nearly uniform ring around the solar wind peak which does not yet merge into the solar wind in order to form a smooth tail on the solar wind distribution. Rather, it remains to be separated from the solar wind, showing that the reflected ions have been scattered nearly uniformly in velocity.

This scattering results from both the adding of the lower velocity part of the reflected ion distribution being swept towards the shock and the vulnerability of the reflected ions against excitation and scattering of waves. The foreshock contains two ion components. One is the ions of the foreshock boundary, which become convected toward the shock. However, at the same time the shock still reflects ions upstream, which try to propagate into the solar wind. This, however, is not easily possible because

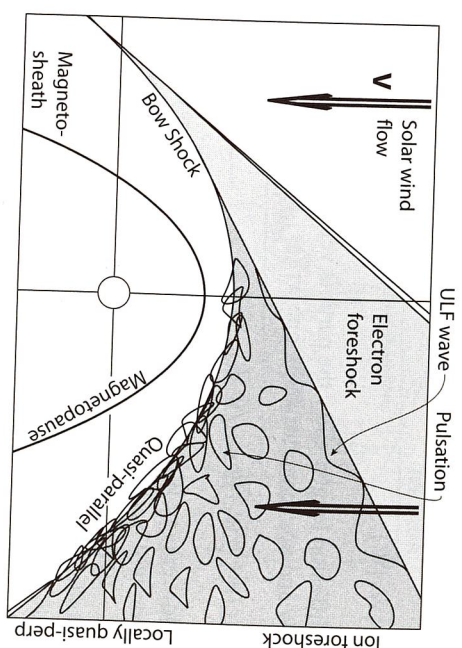


Figure 13.18: Quasi-parallel supercritical shocks reform by accumulation of upstream magnetic pulsations convected into the shock from the ion foreshock, thereby causing an irregular shock structure and contributing to the turning of the magnetic field into a direction to the shock normal that is more perpendicular, i.e., the magnetic field is more parallel to the shock surface with the shock surface itself becoming very irregular. It is shown schematically that the pulsations grow out of the small amplitude upstream waves which are generated in the broad ULF-wave-unstable region in greater proximity to the ion-foreshock boundary. When the ULF waves evolve to large amplitude and form localised structures and pulsations, these are convected toward the shock, grow, steepen, overlap, accumulate, and lead to the build up of the irregular quasi-parallel shock structure which overlaps into the downstream direction. Downstream turbulence behind quasi-parallel supercritical shocks is thus large due to pulsations that emerge from the shock and move downstream.

of the turbulent structure of the foreshock magnetic fields. These ions thus penetrate upstream into the foreshock in a diffusive wave, in which the foreshock waves are actively involved.

The interaction with the waves indicates that the motion of the reflected ions is a combination of convection and diffusive scattering into upward direction in the waves generated close to the shock. The spatial decay into the upstream direction of the diffuse ion density,

$$n_i(W, z) \sim \exp[-z/L(W)], \quad (13.29)$$

differs for particles of different energy, W . The e-folding distance, $L(W) \sim W$, increases linearly with energy, suggesting that low energy reflected particles are practically confined to the shock and do not diffuse upstream. The higher the ion energy, the deeper the ions can overcome the convection and diffusively penetrate back into the upstream flow. In contrast to the ion beam, whose source is at the quasi-perpendicular to quasi-parallel shock boundary, the source of the *diffuse* ions is located at the quasi-parallel shock.

The e-folding distance for the diffuse ions is given by:

$$L(W) = \kappa_{||}(W)/V_1, \quad (13.30)$$

with spatial diffusion coefficient

$$\kappa_{\parallel}(W) = \frac{1}{3} \nu \ell_{\parallel}(W), \quad (13.31)$$

where ℓ_{\parallel} is the diffusion length, and ν the particle velocity. From the balance between convective inflow and upstream diffusion, one writes

$$\ell_{\parallel}(E) = 3L(W) \sqrt{W_1/W} \sim \sqrt{W W_1}, \quad (13.32)$$

with upstream flow energy W_1 . In the solar wind the flow energy is a few keV, and a 20-keV diffuse ion will have a typical parallel diffusion length (or diffusive mean free path) of $\ell_{\parallel} \sim (1-2) R_E$, a rather short upstream distance from the bow shock only, orders of magnitude shorter than the collisional mean free path of an ion. Hence, the diffusion estimate suggests that strong wave-particle interactions in the shock transition are responsible for the scattering and acceleration of the diffuse particle component. The corresponding upstream-ion collision frequency, $\nu_{ci} \approx \nu/\ell_{\parallel}$, for the 20-keV-upstream ions in the solar wind yields $\nu_{ci} \sim 0.2$ Hz, being comparable to the ion cyclotron frequency, $\omega_{ci}/2\pi \approx (0.1-0.3)$ Hz, in the $B \approx 8$ nT upstream to $B \approx 30$ nT shock ramp magnetic field in observations.

13.3.2 Quasi-parallel Shock Reformation

In quasi-parallel supercritical shocks there is not such an obvious stringent distinction between the region upstream of the shock and the shock itself as there is in quasi-perpendicular shocks. Strictly speaking, the foreshock and the shock itself cannot be considered separately. This is due to the presence of the reflected and diffuse particle components in the foreshock. These are the sources of a large number of waves, which are excited in the foreshock by an ion-ion instability between the solar wind flow and the isotropic though inhomogeneous diffuse upstream ion component. The excited waves are, however, slow in comparison to the super-Alfvénic solar wind. This implies that they cannot propagate upstream from the location of their excitation. On the contrary, though flowing against the solar wind they become swept downstream against the shock and grow. The interaction of these large-amplitude electromagnetic ion waves – called foreshock magnetic pulsation – with the shock is one of the main issues in quasi-parallel shock physics.

Role of Upstream Pulsations

The shock radiates energy away towards upstream in the reflected diffuse particle component, which exhibits a steep upstream ion-density gradient. On their paths, when approaching the shock, the low-frequency electromagnetic ion-plasma waves that have been excited in the foreshock by the electromagnetic ion-ion instability encounter the diffuse ion gradient and experience the exponentially increasing number of diffuse particles the shorter the distance between the waves and the shock becomes. Interacting with the ever denser diffuse ions, the electromagnetic waves

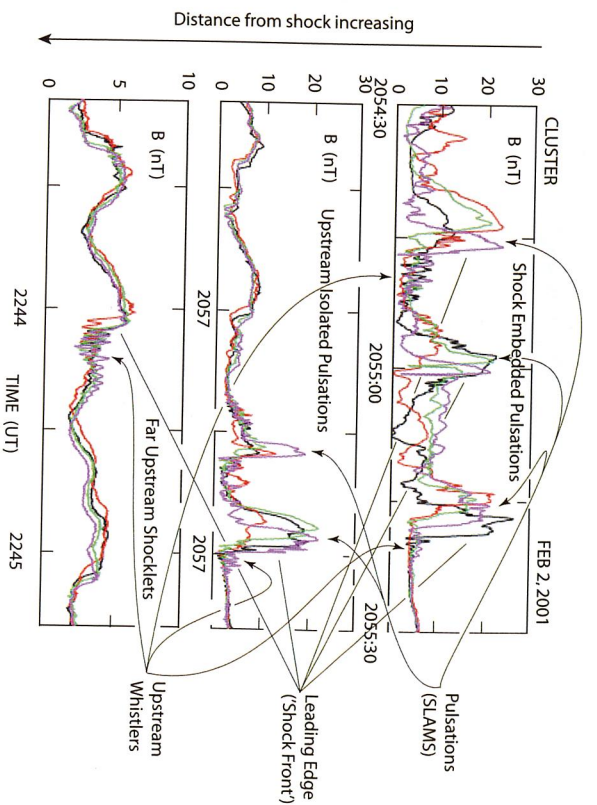


Figure 13.19: Magnetic field of pulsations in the quasi-parallel foreshock for the 4 Cluster (colour coded) spacecraft. *Top:* Accumulated pulsations in the shock transition being of small scale and large amplitude. *Centre:* Isolated pulsation at larger distance seen almost simultaneously at the 4 spacecraft being of larger size but lower amplitude. *Bottom:* Far upstream shocklet and ultra-low-frequency waves with attached upstream whistlers.

become strongly amplified, until reaching large amplitudes of the same order as the background solar wind magnetic field in the foreshock.

At this stage they undergo nonlinear deformation and steeping, forming magnetic foreshock pulsations of larger tangential than normal wavelengths. Their \mathbf{k} -vectors turn away from the background solar wind magnetic field when growing nonlinear and the components of \mathbf{k} assume comparable values parallel to \mathbf{B} and parallel to the shock normal \mathbf{n} .

Close to the shock, where the backstreaming ion density is highest, the waves have short wavelengths, and \mathbf{k} is almost parallel to \mathbf{n} , implying that the magnetic field of the waves has turned away from the quasi-parallel direction and has become almost quasi-perpendicular. This has a very strong effect on the evolution of quasi-parallel shocks, which we are going to explain below.

Before proceeding, we show high Mach number quasi-parallel shock simulations in Fig. 13.17, in which these effects are seen. In these simulations reflected ions were artificially injected with the same Mach number as the incoming flow, but with much higher temperature, $v_{thi} \approx 14 v_A$, forming an initially spatially uniform ion component.

The upstream waves have two components, b_z, b_y , are of low amplitude at large distance from the shock, but reach very large amplitudes simultaneously in both com-

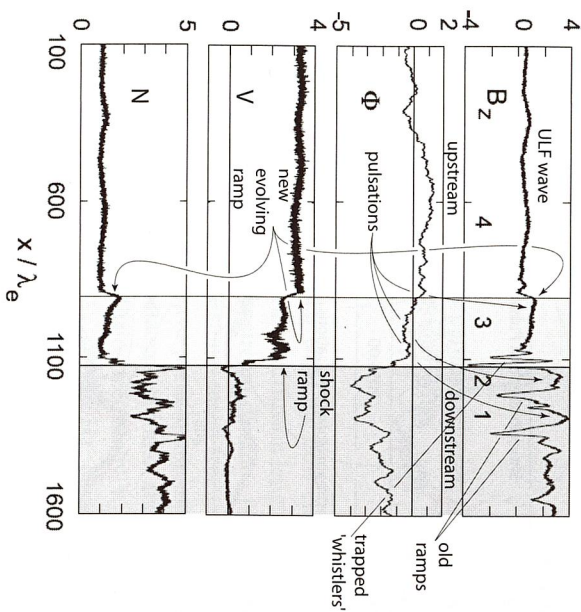


Figure 13.20: 1D full particle PIC simulations of quasi-parallel shock evolution: Magnetic field B_z , electric potential Φ , flow velocity V , density N (in simulation units). Numbers indicate 3 pulsations. Pulsation 1 was the old shock. Pulsation 2 is the actual shock (coinciding with drop in V to zero and steep increase in density and potential). Pulsation 3 is just evolving. Number 4 will become a pulsation. The actual shock ramp has some trapped whistlers.

ponents during shock approach, while bending and assuming a structure in z -direction that is different from the regular elongated shape at large distance.

This deformation of wave front implies that the shock has attained structure on the surface in both directions, x and z , and is not planar anymore. The shock becomes locally curved on the scale of the shock-tangential wavelength. The waves deform the shock and are of the same amplitude as the shock ramp. They become gradually indistinguishable from the shock. The shock is, so to say, the first and largest-amplitude upstream magnetic pulsation. In addition, the quasi-parallel shock-magnetic field is not coplanar, because the waves have contributed a substantial component, b_y , that points out of the coplanarity plane.

Reformation

Quasi-parallel shock reformation and much of its physics is predominantly due to the presence of the large-amplitude and spatially distinct upstream waves. The important conclusion is that large-amplitude upstream pulsations are the physical generators of the shock.

The presence of large amplitude magnetic pulsations lets the quasi-parallel shock locally change its character. It becomes variable in time and position along the shock

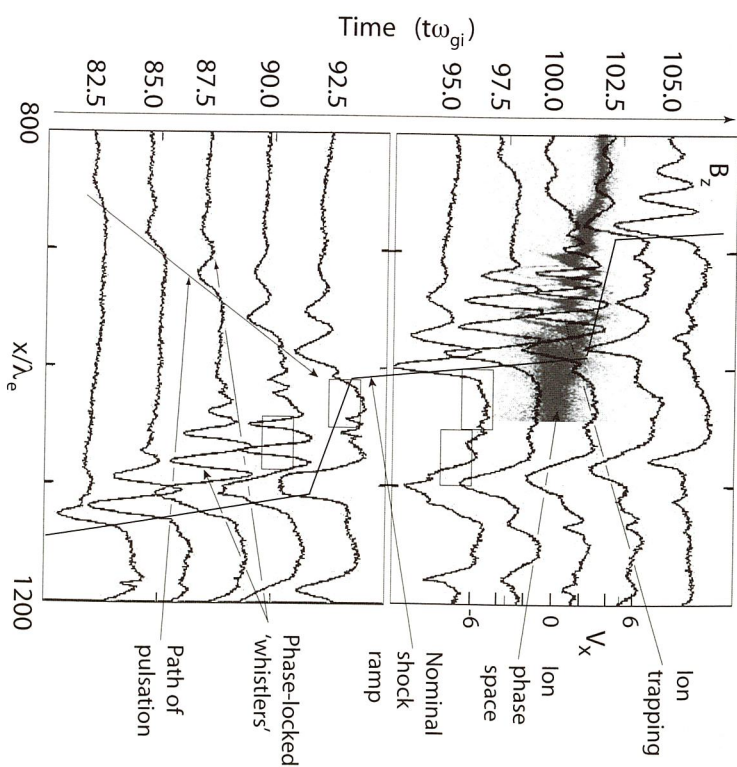


Figure 13.21: Magnetic field B_z in simulation frame for subsequent simulation times (shifted upward by $\Delta t \omega_{gi} = 2.5$). The shock moves to the left into the upstream direction. Reformation results from exchange with incoming pulsation. The magnetic field trace at time $t \omega_{gi} = 100$ has been overlaid on the ion phase space at this time. Heavy steps show location of nominal shock ramp moving upstream until new pulsation arrives and it suddenly jumps forward by roughly $100 \lambda_e$. A pulsation arrives at the shock at $t \omega_{gi} = 92.5$ to take over the role of the shock. In the minima of the 'whistler' field fluctuations ($t \omega_{gi} = 100$) ions are trapped, forming vortices in phase space centred around local minima of the electric potential Φ (not shown). The little boxes indicate where particle phase space distributions have been determined.

surface and – on the smaller scale close to the shock transition – is 'less quasi-parallel' (or 'more perpendicular'), i.e., the shock-normal angle, Θ_{Bn} , has increased on the scale of the upstream waves because of the presence of the out-of coplanarity-plane component that is introduced by the upstream waves.

This can be realised from the right part of Fig. 13.17, where the evolution of the local shock normal angle, Θ_{Bn} , is plotted for two simulations of different initial quasi-parallel shock normal angle in the course of the approach of a spectrum of upstream large amplitude waves which have been generated self-consistently. When approaching close to the shock ramp, Θ_{Bn} rapidly increases from quasi-parallel to quasi-perpendicular in both cases, until it is found deep in the domain of quasi-perpendicular shocks. The evolution of Θ_{Bn} is not smooth.

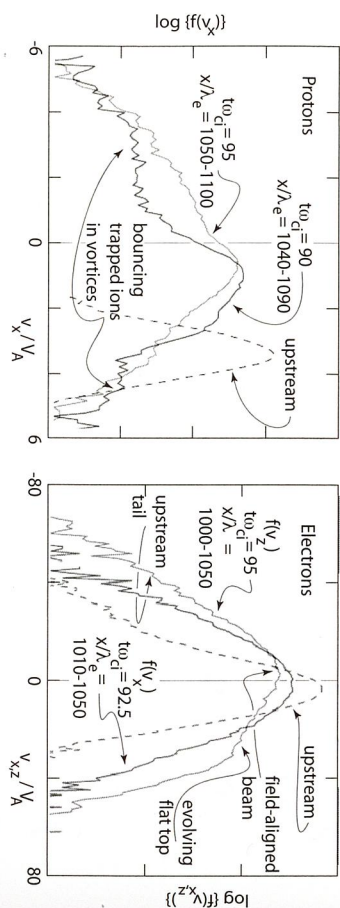


Figure 13.22: Velocity distributions for different phases of shock evolution taken in the boxes of Fig. 13.21. *Left:* Proton distributions at $t_{0i} = 90, t_{0e} = 95$. The first period is in the arriving pulsation. The upstream distribution is heated with upstream tail due to trapped ions. At $t_{0i} = 95$, the trapped hot ion distribution damps the waves. The incident plasma is slowed down. *Right:* Electron distributions $f_e(v_x)$ at $t_{0e} = 92.5$ and $f_e(v_x)$ at $t_{0e} = 95$ in the new shock, built up from a fresh pulsation and in the well-developed shock but along the main magnetic field, respectively. The parallel distribution is non-symmetric, heated, has an upstream tail, formation of a flat top, and a remaining upstream-beam-like part similar to measured.

Transition to local quasi-perpendicularity occurs for the initially nearly parallel case, right at the nominal shock ramp on a short scale, while for the initially more inclined quasi-parallel case it already occurs at an upstream distance of about $\sim 100\lambda_i$ from the shock. The latter case is sufficiently far away for the upstream flow ions to feel the change in the shock normal. This transition, being on the ion scale, implies that in the region close to the shock, the upstream-flow ions occasionally experience the shock as being quasi-perpendicular and become reflected. This is the way in which the quasi-parallel shock regenerates its upstream reflected ion component.

The behaviour of the shock normal angle gives a rather clear identification of the location of the shock transition in the quasi-parallel case, as indicated on the right in Fig. 13.17 by shading. Three distinctions can be noticed:

- at larger initial shock-normal angles, the transition to quasi-perpendicular angles occurs earlier, i.e., farther upstream than for nearly parallel shocks. This is due to the strong effect of the large amplitude upstream waves;
- at larger initial shock normal angles, the quasi-perpendicular shock transition is considerably broader than for nearly parallel shocks, i.e., it extends farther downstream before the main quasi-parallel direction of the magnetic field in the downstream region takes over again and dominates the direction of the magnetic field;
- at an initial shock-normal angle of 20° , this region is roughly $\sim 150\lambda_i$ wide, implying that the magnetic field direction behind a quasi-parallel shock remains to be quasi-perpendicular over quite a long downstream distance measured from the shock ramp. For the nearly parallel shock this volume is only about $\sim 50\lambda_i$ wide.

Three representative examples of such upstream waves which support the above theoretical inference have been plotted in Fig. 13.19. The shock region consists of

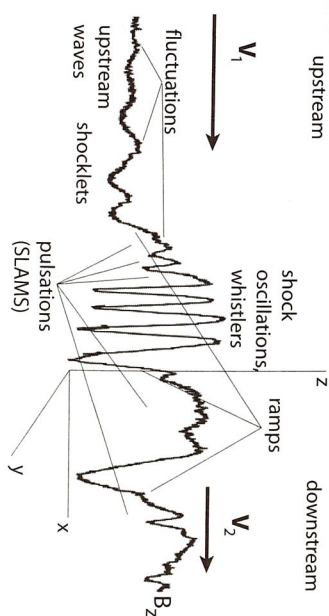


Figure 13.23: Schematic one-dimensional profile taken along the nominal instantaneous shock normal of a supercritical quasi-parallel shock, as seen in the magnetic field component B_z . This is the analogue to the quasi-perpendicular shock profile. It shows the main features in the vicinity of the quasi-parallel shock transition: the large amplitude upstream waves with the turbulent fluctuations on top of the waves, the formation of shocklets, i.e., steep flank formation on the waves exhibiting small-scale fluctuations on top of the wave, which act already like small shocks, very-large amplitude pulsations (magnetic pulsations) which turn out to be the building blocks of the shock, multiple shock-ramps at the leading edges of the pulsations belonging to diverse ramp-like steep transitions from upstream to downstream, lacking a clear localisation of the shock transition and any attached phase-locked whistlers (Note that the entire figure is, in fact, the shock transition, as on this scale no clear decision can be made as to where the shock ramp is located.) Not shown here are the out of plane oscillations of the magnetic field that accompany the waves. The particle phase space is not shown.

many embedded magnetic pulsations of very large amplitudes, having steep flanks and irregular shapes. They exhibit higher frequency oscillations in the whistler mode, sitting on their feet or shoulders. Pulsations in the shock are short-scale; the 4 different Cluster spacecraft – at spacecraft separation < 1000 km – do not observe a coherent picture of a particular pulsation. The magnetic field directions differ from spacecraft to spacecraft and from pulsation to pulsation, and even for one pulsation at its front and trailing edges, and the magnetic normal directions change on the short spatial scales across a single pulsation.

Full particle PIC simulations of quasi-parallel shock reformation, shown in Fig. 13.20, strongly support this picture. On the left the reformation of the shock due to exchange of pulsations is shown. On the right this process is followed in time. The nominal shock front progresses stepwise in an upstream direction when an old magnetic pulsation is replaced by one that is newly arriving.

In the phase space, the magnetic oscillations are well correlated with ion holes, with the field maxima coinciding with the vertexes and the minima corresponding to the centres of the holes, i.e., to the locally largest spread in the ion distribution or, in other words, the locally highest ‘ion temperatures’. The evolution of the corresponding velocity distributions for ions and electrons in this reformation process is given in Fig. 13.22. Heating of ions and electrons takes place in different phases, and there is an indication of acceleration of an electron beam.

Quasi-parallel shocks form and reform in the course of an interplay between the shock-produced upstream diffuse energetic-ion component and the magnetic pulsa-

tions which grow out of the wave-excited upstream waves and are amplified in the interaction with the diffuse ions during their approach of the shock. On the other hand and supporting the above formulated view, quasi-parallel supercritical (high Mach number) shocks do not reform in the absence of diffuse upstream ions and the waves that are excited by them. A graphical summary of the structure of quasi-parallel shocks is given finally in Fig. 13.23.

13.4 Concluding Remarks

In this last chapter we have given an application of the physics of a space plasma to one of the most interesting and most complex problems in space plasma physics, the formation of subcritical and super-critical collisionless shocks.

This problem has been chosen because it paradigmatically contains all of plasma physics: fluid physics, which provides the global jump conditions; single particle theory, which allows to distinguish between quasi-parallel and quasi-perpendicular collisionless shocks in the supercritical case; steeping of waves and the achievement of a stationary state in balance of steeping and dispersion in the case of subcritical solitary waves, which can be described by Sagdeev's pseudo-potential; the insufficient role of dissipation in shock formation, in particular in the case of super-critical shocks; and the problem of instability and wave generation.

Because in shocks, entropy is produced continuously, collisionless super-critical shocks cannot be and are not in thermodynamic equilibrium. They are continuously forming and reforming. This process is one of the most interesting in the entire physics of collisionless shocks, and we have focussed on it. The surprising result is that reform is completely different for quasi-perpendicular and quasi-parallel shocks.

Both kinds of collisionless shocks reform with the help of particle reflection. This is necessary for reasons of entropy, because the time to generate sufficient diffusion in order to prevent shock wave breaking in the collisionless super-critical plasma is too long. The shock has simply not enough time to digest the inflowing amount of energy which it can get rid of only by not permitting the excess energy to pass the shock transition. In other words, the shock rejects the excess energy inflow by reflecting its carriers, a large fraction of upstream ions, back upstream.

Quasi-perpendicular shocks use these reflected particles to form a shock foot and shock-foot current, the proper magnetic field of which grows in front of the shock ramp to large amplitudes, until it becomes large enough to start itself reflecting particles. In this way it becomes the new shock front. The quasi-perpendicular shock reforms itself quasi-periodically in this way.

Quasi-parallel shocks, on the other hand, release a large fraction of particles back upstream, forming a shock foreshock which contains high fluxes of those upstream particles. These upstream particles create a high level of upstream low frequency electromagnetic plasma waves via an ion-ion beam instability. Since these newly generated waves have low phase and group speeds, they cannot travel far upstream, but

become convected into the shock ramp, grow during the convection time, and evolve into large-amplitude magnetic foreshock pulsations.

It is these pulsations which reform the shock by becoming the shock along small tangential patches of the shock surface. In this process the old shock front in the patch is ejected downstream, where it becomes the main component of the downstream large amplitude turbulence, as, for instance, in the magnetosheath, while the shock is reformed by the pulsation that had newly arrived at this particular patch. For this reason quasi-parallel shocks are very variable and in fact turbulent. For this reason they can form under collisionless conditions when fluid shocks cannot exist. From this statement we learn, in addition, that any collisionless super-critical shocks will always be magnetised, as only then can they form and reform which is the condition for their existence.

Probably, in the absence of an initial magnetic field, the shock will take care of generating its own field in some way. One way is through a violent Weibel instability.

Having presented these basic ideas, mostly by quoting numerical simulations and not by deductively deriving them from basic principles, we should note that we have not only suppressed their deduction but also kept silent about a large number of other effects which are related to collisionless shocks. Among such effects are the production of entropy in general and the production of dissipation, which we did not discuss, as this is a main and unresolved question of thermodynamics when dealing with collisionless shocks.

Other important effects include the generation of radiation by shocks. Astrophysical shocks and also some of the shocks in the heliosphere, like Earth's and Jupiter's bow shocks, as well as interplanetary shocks, are strong banded radiators and are visible in radiation of plasma and electromagnetic free space waves. These processes are related to plasma instability and nonlinear interaction.

Finally, one of the most interesting questions is whether shocks can accelerate ions and electrons to the high energies which are occasionally observed in space. Customarily, shocks are made responsible for the generation of very high energy particles like cosmic rays and solar energetic particles. The bow shock, on the other hand, has not been found to be a strong accelerator. The bow shock is capable of injecting particles and reflecting particles, but the energies obtained are very moderate. Why this is so remains unclear. Possibly the geometric size of the bow shock is too small, the size of the transition region, the magnetosheath, is too narrow, and the level of turbulence in the magnetosheath is too low for the shock and its environment to become a strong particle accelerator. In all the mentioned processes waves are involved, and we will have to await much larger scale simulations in three dimensions until we will be in the position to answer some of the related questions.

We note, finally, that the figures of this chapter have been taken from Reference [1], if not indicated otherwise.

References

The first and classic general treatment of the physics of collisionless shocks, going far beyond earlier hydrodynamic theories, but with no emphasis on space physics, is the comprehensive and still valid review article by Sagdeev [6] of 1966. This article is full of important ideas and deep insight into the shock problem. A first and highly mathematical treatise of plasma instabilities related to the formation of solitons, also including anomalous dissipation to obtain shocks, is found in the short monograph [5], written five years later, lacking, however, the depth of understanding as contained in [4]. Useful observational and theoretical accounts on various main and scattered aspects of collisionless shocks, summarising the state of the art in 1985 can be found in the two AGU conference proceedings [7,9], which, however, are rather inhomogeneous and of highly variable importance. So are the two Cospas [4] and AIP [3] conference proceedings of 1995 and 2005, respectively. A recent, more complete and systematic account of the current knowledge on non-relativistic collisionless shock physics including applications to the shocks in the heliosphere can be found in [1]. For application aspects to astrophysics, one may consult [9]. An account of relativistic shocks is contained in [2].

- [1] A. Balogh and R. A. Treumann, *Physics of Collisionless Shocks, The Space Plasma Shock Waves* (Springer Verlag, Heidelberg-New York, 2012).
- [2] A. M. Bykov and R. A. Treumann, Fundamentals of collisionless shocks for astrophysical application: 2. Relativistic shocks, *Astron. Astrophys. Rev.* **19**, 42–108 (2011).
- [3] G. Li, G. P. Zank, and C. T. Russell, eds. *The Physics of Collisionless Shocks*, AIP Conference Proceedings Vol. 781 (American Institute of Physics, Melville, NY, 2005).
- [4] C. T. Russell, ed. *Physics of Collisionless Shocks*, Adv. Space Phys. **15**, Number 8/9 (Cospas-Pergamon-Elsevier, Oxford, 1975).
- [5] D. A. Tidman and N. A. Krall, *Shock Waves in Collisionless Plasmas* (Wiley-Interscience, New York, NY, 1971).
- [6] R. Z. Sagdeev, in *Rev. Plasma Phys. Vol. 4*, ed. M. A. Leontovich (Consultants Bureau, New York, NY, 1966), pp. 23–92. (1989).
- [7] R. G. Stone and B. T. Tsurutani, eds. *Collisionless Shocks in the Heliosphere, A Tutorial Review* (AGU Monograph 34, AGU, Washington, DC, 1985).
- [8] R. A. Treumann, Fundamentals of collisionless shocks for astrophysical application: Non-relativistic shocks, *Astron. Astrophys. Rev.* **17**, 409–535 (2009).
- [9] B. T. Tsurutani and R. G. Stone, eds. *Collisionless Shocks in the Heliosphere, Reviews of Current Research* (AGU Monograph 35, Washington, DC, 1985).

REFERENCES

Some selected additional more specialised references:

- S. D. Bale et al., (*Astrophys. J.*) **575**, L25–L28 (2002).
- S. D. Bale, F. S. Mozer, and T. S. Horbury, *Phys. Rev. Lett.* **91**, 265004 (2003).
- S. D. Bale and F. S. Mozer, *Phys. Rev. Lett.* **98**, 205001 (2007).
- D. Biskamp, *Nuclear Fusion* **13**, 719–740 (1973).
- D. Burgess et al., *Space Sci. Rev.* **118**, 205–222 (2005).
- M. Hoshino and T. Terasawa, *J. Geophys. Res.* **90**, 57–64 (1985).
- C. Kennel, J. P. Edmiston, and T. Hada, in *Collisionless Shocks in the Heliosphere: A Tutorial Review*, R. G. Stone and B. T. Tsurutani (AGU, Washington, DC, 1985) pp. 1–36.
- A. Kis et al., *Geophys. Res. Lett.* **31**, L20801 (2004).
- E. A. Lucek et al., *Ann. Geophysicae* **20**, 1699–1710 (2002).
- E. A. Lucek et al., *J. Geophys. Res.* **109**, A06207 (2004).
- E. A. Lucek et al., *J. Geophys. Res.* **113**, A07S02 (2008).
- S. Matsukiyo and M. Scholer, *J. Geophys. Res.* **111**, A06104 (2006a).
- S. Matsukiyo and M. Scholer, *Adv. Space Res.* **38**, 57–63 (2006b).
- M. Scholer, I. Shinohara, and S. Matsukiyo, *J. Geophys. Res.* **108**, 1014 (2003).
- S. J. Schwartz, M. F. Thomsen, and J. T. Gosling, *J. Geophys. Res.* **88**, 2039–2047 (1983).
- S. J. Schwartz and D. Burgess, *Geophys. Res. Lett.* **18**, 373–376 (1991).
- S. J. Schwartz, D. Burgess, and J. J. Moses, *Ann. Geophysicae* **14**, 1134–1150 (1996).
- N. Sckopke et al., *J. Geophys. Res.* **88**, 6121–6136 (1983).
- N. Shinada and M. Hoshino, *Astrophys. J.* **543**, L67–L71 (2000).
- N. Shinada and M. Hoshino, *J. Geophys. Res.* **110**, A02105 (2005).
- E. S. Weibel, *Phys. Rev. Lett.* **2**, 83–84 (1959).
- P. H. Yoon, *J. Geophys. Res.* **99**, 23,481–23,488 (1994).